NOVA SCHOOL OF SCIENCE & TECHNOLOGY

DEPARTMENT OF
MECHANICAL AND INDUSTRIAL ENGINEERING

DANIEL ALEXANDRE ESTIMA AMENDOEIRA
BSc in Mechanical Engineering

EVALUATION OF THE INFLUENCE OF NOZZLE COOLING DURING THE HOT FORGING WIRE AND ARC ADDITIVE MANUFACTURING PROCESS

INTEGRATED MASTER IN MECHANICAL ENGINEERING

NOVA University Lisbon

September, 2023

NOVA SCHOOL OF SCIENCE & TECHNOLOGY

DEPARTMENT OF
MECHANICAL AND INDUSTRIAL ENGINEERING

EVALUATION OF THE INFLUENCE OF NOZZLE COOLING DURING THE HOT FORGING WIRE AND ARC ADDITIVE MANUFACTURING PROCESS

DANIEL ALEXANDRE ESTIMA AMENDOEIRA

BSc in Mechanical Engineering

Adviser: Valdemar Rebelo Duarte
Invited Assistant Professor, NOVA University Lisbon

Co-advisers: Telmo Jorge Gomes dos Santos
Full Professor, NOVA University Lisbon

Examination Committee:

Chair: Nuno Alberto Marques Mendes,
Assistant Professor, NOVA University Lisbon

Rapporteurs: João Pedro de Sousa Oliveira,
Assistant Professor with Habilitation, NOVA University Lisbon

Adviser: Valdemar Rebelo Duarte,
Invited Assistant Professor, NOVA University Lisbon

INTEGRATED MASTER IN MECHANICAL ENGINEERING

NOVA University Lisbon
September, 2023

Evaluation of the influence of nozzle cooling during the Hot Forging Wire and Arc Additive Manufacturing process

To my family and friends

ACKNOWLEDGMENTS

These five years of academic life have culminated in this work, in which I have devoted all my effort and commitment. But it is the people who surround me that make it all possible.

I would like to start by thanking my supervisor, Professor Valdemar Duarte, for all his knowledge, availability and support throughout this work and for giving me the opportunity to deepen my knowledge.

To my co-supervisor, Professor Telmo Santos, for his expertise and know-how, and for continuously encouraging me to deepen my knowledge and to improve myself every day.

My deepest gratitude to my precious friends Francisco Baptista and Rodrigo Confraria for their long and true friendship over the last few years, for all the deep conversations we've had and for what is yet to come.

To my good homies, Hugo Bastos and João Domingues, a warm thank you for your companionship and late-night talks.

A very special thanks to my great friend João Marto, with whom I've lived unforgettable experiences and stories to tell.

To my dear friends Alumina (Al_2O_3) for all the wonderful meetings and memories that I treasure. Together, we have walked a beautiful academic path, with lots of support and love for each other.

My special gratitude to my better half, the one who makes me a better man and with more certainties. Raquel, thank you for all the calm and peace you bring me. I hope to be able to reciprocate all the continuous support you give me.

To my beloved parents and sister, for providing me with the best education and childhood I could have ever asked for and for all their love and unconditional support throughout my journey.

ABSTRACT

Additive manufacturing processes have emerged to complement the conventional processes, allowing the production of components with high geometrical complexity and reducing raw material waste. Among additive manufacturing processes for metals, the Wire and Arc Additive Manufacturing (WAAM) technology has aroused particular interest due to its capacity to produce large-scale components in useful time. However, there are common limitations in additive manufacturing processes that need to be overcome in order to industrialize the process, particularly the formation of porosities, coarse microstructures and anisotropy.

This work focused on the design and study of a new variant of WAAM technology that combines the advantages of mechanical deformation with forced cooling.

This variant consisted of hot forging between the deposition of each layer using a cooled hammer with the aim of increasing the cooling rate of the material, reducing the peak temperature, promoting grain refinement and reducing the anisotropy. Samples of a high-strength low-alloy (HSLA) steel were produced, with and without the use of the hammer, on which uniaxial tensile tests, microhardness, electrical conductivity and optical microscopy were performed. Moreover, thermography was used to analyze the thermal cycles that occurred in the material.

It was found that hot forging contributes to refining the microstructure and reducing the anisotropy of the material. Combining the cooling system with hot forging led to a 77% reduction in hammer temperature and a 12% reduction in peak temperature and has helped to increase the material's cooling rate. After the tensile tests, the samples registered an increase in their mechanical strength and all exhibited ductile fracture. Furthermore, the use of the hammer caused a considerable reduction in the quantity and size of pores.

Keywords: WAAM, hot forging, cooling, HSLA steel, microstructure, grain refinement

RESUMO

Os processos de fabrico aditivo surgiram com o intuito de complementar os processos convencionais, permitindo a produção de componentes com elevada complexidade geométrica e reduzindo o desperdicio de matéria-prima. Entre os processos de fabrico aditivo de metais, a tecnologia Wire and Arc Additive Manufacturing (WAAM) tem suscitado particular interesse, devido à sua capacidade para produzir componentes de grande escala em tempo útil. Contudo, existem limitações comuns nos processos de fabrico aditivo que necessitam de ser ultrapassadas para viabilizar a industrialização do processo, nomeadamente a formação de porosidades, microestruturas grosseiras e anisotropia.

Este trabalho incidiu sobre a conceção e estudo de uma nova variante da tecnologia WAAM que combina as vantagens da deformação mecânica com o arrefecimento forçado.

Esta variante consistiu no forjamento a quente entre a deposição de cada camada através de um martelo arrefecido com o objetivo de aumentar a taxa de arrefecimento do material, reduzir a temperatura de pico, promover o refinamento de grão e reduzir a anisotropia. Produziram-se amostras de um aço de alta resistência e baixa liga, com e sem a utilização do martelo, nas quais foram realizados ensaios de tração uniaxial, microdureza, condutividade elétrica e microscopia ótica. Adicionalmente, recorreu-se à termografia para analisar os ciclos térmicos que atuaram sobre o material.

Concluiu-se que o forjamento a quente contribui para refinar a microestrutura e reduzir a anisotropia do material. A combinação do sistema de arrefecimento com o forjamento a quente provocou uma redução de 77% na temperatura do martelo e de 12% na temperatura de pico, e contribuiu para aumentar a taxa de arrefecimento do material. Após os ensaios de tração, observou-se que as amostras registaram um aumento na resistência mecânica e todas apresentaram fratura dúctil. Verificou-se também que a utilização do martelo provoca uma redução considerável na quantidade e dimensão dos poros.

Palavras-chave: WAAM, forjamento a quente, arrefecimento, aço de alta resistência e baixa liga, microestrutura, refinamento de grão

CONTENTS

LIST OF FIGURES

LIST OF TABLES

ACRONYMS

AF	Acicular Ferrite
AM	Additive Manufacturing
CCT	Continuous Cooling Transformation
CTWD	Contact Tip to Work Distance
DED	Directed Energy Deposition
DED-arc	Directed Energy Deposition-arc
FDM	Fused Deposition Modelling
FS (A)	Ferrite with Second phase Aligned
GF	Grain Boundary Ferrite
GMAW	Gas Metal Arc Welding
GTAW	Gas Tungsten Arc Welding
HAZ	Heat Affected Zone

HF-WAAM	Hot Forging Wire and Arc Additive Manufacturing
HSLA	High Strength Low Alloy
ISO	International Organization for Standardization
MAG	Metal Active Gas
MHP	Machine Hammer Peening
MIG	Metal Inert Gas
NDT	Non-Destructive Testing
PAW	Plasma Arc Welding
PBF	Powder Bed Fusion
PF	Polygonal Ferrite
SEM	Scanning Electron Microscope
TIG	Tungsten Inert Gas
TPU	Thermoplastic Polyurethane
TS	Travel Speed
UTS	Ultimate Tensile Strength
WAAM	Wire and Arc Additive Manufacturing
WFS	Wire Feed Speed

1 INTRODUCTION

1.1 MOTIVATION

The fourth industrial revolution involves the integration of advanced technologies across industries to increase automation, enabling greater flexibility, customization and process efficiency. Additive Manufacturing (AM) processes have emerged to complement conventional manufacturing processes, allowing the production of complex geometry components in a short period of time with reduced waste of raw materials. These advantages have aroused the interest of several researchers and industries and, as a result, additive manufacturing processes have experienced a notorious evolution over the past few years.

Among the metal AM processes, Wire and Arc Additive Manufacturing (WAAM) has been of particular interest due to its ability to produce large components in a short time frame and with reduced costs. However, there are some constraints that are common to most AM processes, namely porosity formation and coarse microstructures oriented in a preferential direction, causing anisotropy in some mechanical properties.

In order to overcome these constraints and to achieve the industrialization of WAAM, some researchers have developed new process variants, which can be divided into three main categories: mechanical, thermal and chemical. The mechanical variants usually apply plastic deformation between layers, the thermal ones usually resort to cooling between each deposition or heating the substrate. Nevertheless, most of the developed techniques are overly specific and complex and therefore require dedicated systems for their implementation, which makes their industrialization unfeasible.

Therefore, the need to carry out this work was identified, and its main purpose was the development of a device that can be attached to a WAAM torch and perform deformation and cooling simultaneously, thus optimizing the deposition results.

1.2 OBJECTIVES

The primary objective of this dissertation is to design and study a new WAAM process variant, combining the advantages of forced cooling with plastic deformation between the deposition of each layer, to control cooling, improve mechanical properties and mitigate typical process defects, such as porosity formation. To achieve this, some specific objectives were defined:

1) Design and manufacturing of the cooling device.
2) Optimization of process parameters.
3) Sample production with the combination of cooling and forging variants.
4) Preparation and characterization of the produced samples.
5) Evaluation of the effect of forced cooling of the torch nozzle combined with hot forging on the changing microstructure and mechanical properties.

1.3 DOCUMENT STRUCTURE

This dissertation is structured in five chapters.

Chapter 2 reviews the literature on AM processes, with particular focus on the WAAM technology. The process fundamentals and its main constraints are described. Moreover, some techniques to mitigate these limitations are mentioned.

Chapter 3 describes the experimental procedure to produce the samples, including the design of the cooling device and the characterization techniques applied.

Chapter 4 presents the findings from the tests performed, from macro to microscopic perspective, to assess the effect of the cooling system on the cooling rate and properties of the material.

Chapter 5 summarizes the main conclusions drawn from this work and outlines some suggestions for future work.

2 STATE OF THE ART

2.1 ADDITIVE MANUFACTURING

Additive manufacturing is a process that involves the deposition of material in consecutive layers from a three-dimensional digital model. This feature enables the production of customized parts, with high geometrical complexity and reduced waste, without the need to use high-cost tools using the conventional processes.

Furthermore, it is possible to produce parts on demand, reducing the need to stock spare parts, thus reducing the component's lead time [1]. Moreover, the AM processes are automated, which reduces operator intervention. These particularities have prompted interest from various industries to combine this technology with conventional manufacturing processes in order to exploit the advantages of both. Nevertheless, there are some drawbacks, such as the need to perform surface finishing, heat treatment and dimensional correction operations, depending on the material and process used.

Aerospace and aeronautics industries produce parts with high geometric complexity using conventional processes, which generates a lot of material waste and raises the cost of the parts [2]. This has sparked interest in AM processes among these industries with the aim of reducing raw material waste and energy consumption, promoting the environmental sustainability of the manufacturing process and reducing the final cost of the components.

To simplify communication in the additive manufacturing industry and standardize terminology, the ISO 52900:2015 standard was published on the already existing processes and their fundamentals. Table 2.1 presents the seven categories for additive manufacturing processes.

Table 2.1 - Additive manufacturing process categories according to ISO 52900:2015 [3]

Categories	Definition
Binder Jetting	Additive manufacturing process in which a bonding agent is selectively deposited to bond powder particles together
Directed Energy Deposition	Additive manufacturing process in which thermal energy is used to fuse the material as it is deposited
Material Extrusion	Additive manufacturing process where the material is fed through a nozzle or orifice
Material Jetting	Additive manufacturing process where droplets of a photosensitive material are deposited which solidifies under ultraviolet light
Powder Bed Fusion	Additive manufacturing process where thermal energy is used to fuse specific areas of a powder bed
Sheet Lamination	Additive manufacturing process in which thin layers of material are joined to form a part
Vat Photopolymerization	Additive manufacturing process in which a liquid photopolymer is cured through ultraviolet radiation

2.2 ADDITIVE MANUFACTURING FOR METALS

Additive manufacturing involves the use of different materials, including polymers, metals, composites and ceramics. The chosen material depends on the intended application and properties for the part. The main AM processes that use metals as raw material are the Directed Energy Deposition-arc (DED-arc), which utilizes a metallic wire as the feedstock material, and Powder Bed Fusion (PBF), which uses the feedstock in the form of powder. The DED-arc deposition rate of 6 kg/h is considerably higher than the 1 kg/h achieved by the PBF process, thus increasing the lead time [4]. However, the use of wire as the feedstock material results in higher surface waviness and lower dimensional accuracy.

Moreover, the use of metal powder as the raw material makes the process more vulnerable to the formation of defects, particularly porosity [5]. Figure 2.1 a) and Figure 2.1 b) schematically represent the DED and PBF process, respectively.

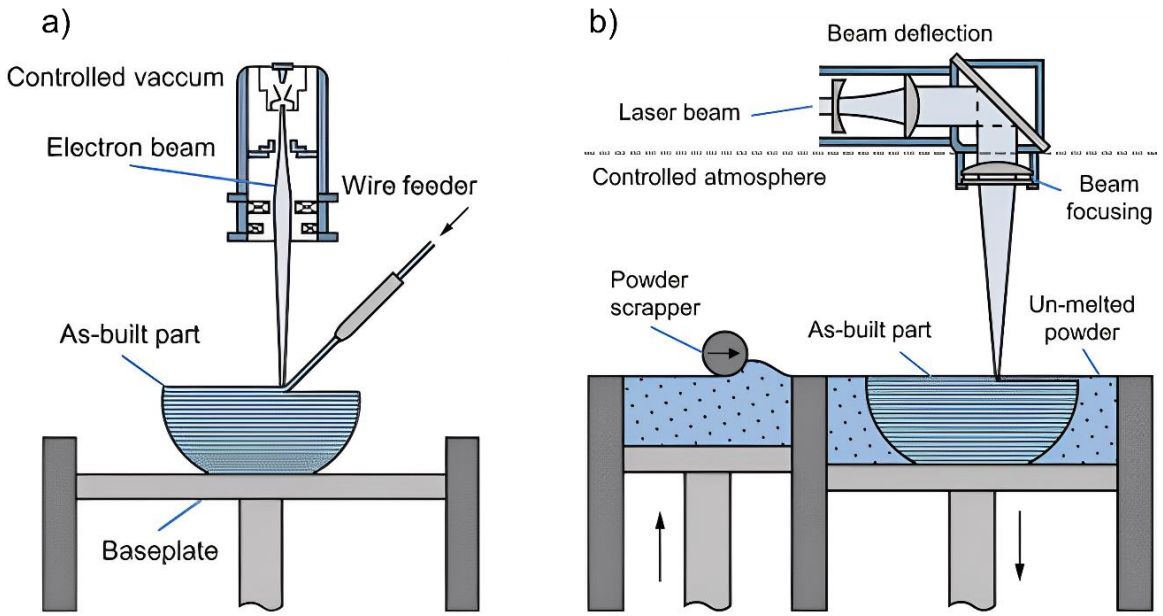

Figure 2.1 - Additive manufacturing of metals: a) Directed Energy Deposition (DED); b) Powder Bed Fusion (PBF) (Adapted from [6])

2.3 WIRE AND ARC ADDITIVE MANUFACTURING

Wire and Arc Additive Manufacturing (WAAM), also known as Directed Energy Deposition-arc (DED-arc), is a metal AM process that uses an electric arc as the energy source and a metallic wire as the feedstock material.

Even though the dimensional accuracy and surface finish quality of the produced parts are lower than those obtained through the PBF process, the high deposition rate of around 6 kg/h allows the production of larger parts in a shorter period of time and at lower costs compared to conventional manufacturing processes in some applications [5].

The WAAM process uses the fundamentals of different electric arc welding processes, such as Gas Metal Arc Welding (GMAW), Gas Tungsten Arc Welding (GTAW) and Plasma Arc Welding (PAW) [5].

GTAW and PAW welding techniques use a non-consumable tungsten electrode to establish the electric arc under the protection of an inert gas. Both processes require an external supply of a filler material. GTAW, also known as Tungsten Inert Gas (TIG), was one of the first arc welding processes to be recognized due to its high precision, with almost no defects, owing to the stability of the electric arc. The difference to the PAW process lies in the fact that PAW comprises the electrode inside the torch, where the electric arc is forced through the nozzle, constricting the arc and thus increasing the energy density. As a result, the arc reaches higher

temperatures (around 15000 ºC [7]) than those achieved in GTAW or GMAW (around 5000 ºC [8]), which implies the need to incorporate an active cooling system.

The advantage of GTAW and PAW processes is the higher arc stability compared to GMAW, which reduces the susceptibility to the formation of defects. To perform additive manufacturing based on these processes, the welding torch is attached to a 3-axis or more movement system. Nevertheless, the fact that GTAW and PAW processes require an external supply of the filler material constitutes a disadvantage because it is necessary to consider the relative position between the filler material and the torch to ensure the consistency of the weld bead geometry, which must be held consistent throughout deposition. For this reason, the production of parts with highly complex geometries demands further automation to rotate the torch according to the direction of deposition.

GMAW, also known as Metal Inert Gas (MIG)/Metal Active Gas (MAG), is the most widely used welding process in WAAM. It uses a consumable electrode in the form of wire, which is protected by an inert or active gas, which also protects the molten pool. Deposition rates range from 1 to 10 kg/h, depending on the material deposited and process parameters, which makes it appropriate for the production of large-scale parts [5]. Figure 2.2 shows the main features of the electric arc welding processes.

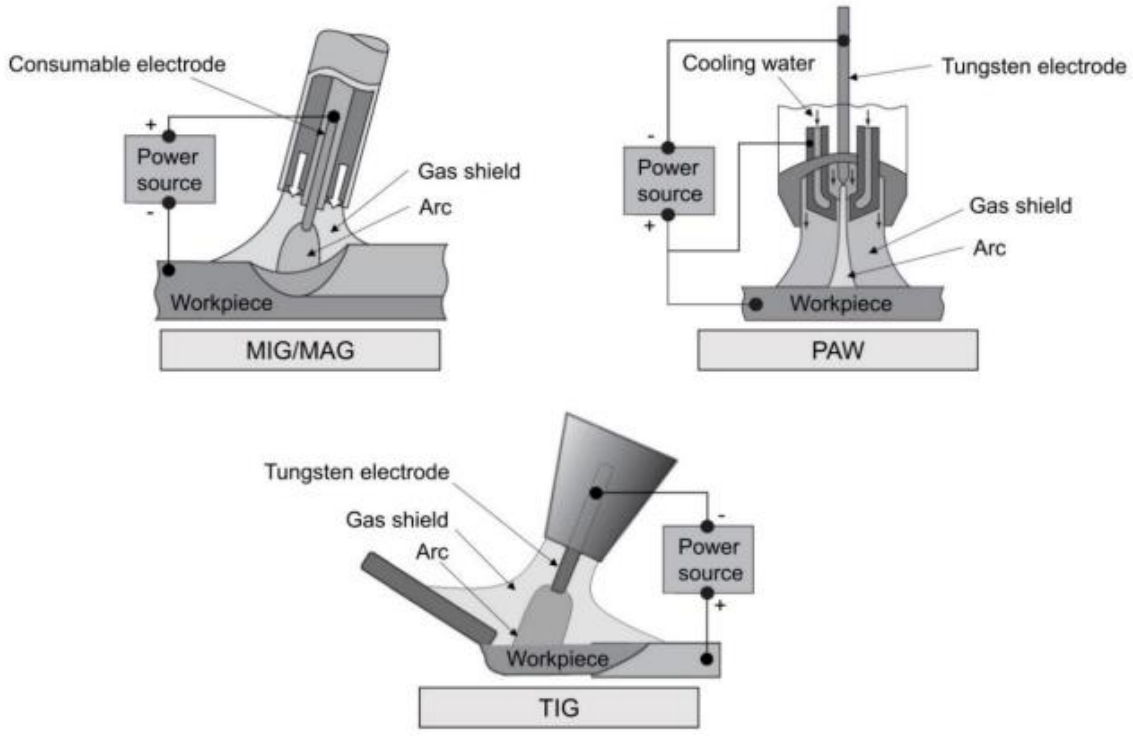

Figure 2.2 - Main features of the MIG/MAG, TIG and PAW processes (Adapted from [9])

2.3.1 PROCESS PARAMETERS

All manufacturing processes involve parameters that directly or indirectly influence the end product. In WAAM, parameter control helps to define the morphology and characteristics of the welding bead. The principal parameters to be considered in the WAAM process are [5]:

- Voltage (V)
- Current intensity (I)
- Travel speed (TS)
- Wire feed speed (WFS)
- Wire diameter
- Welding shielding gas
- Gas flow rate
- Contact tip to work distance (CTWD)

An increase in the current intensity and wire feed speed leads to a wider welding bead and greater penetration. In turn, a higher voltage increases the width of the bead. Similarly, it is possible to increase the penetration of the weld bead by increasing the diameter of the wire, however, greater wire diameters are more susceptible to the formation of defects, especially porosities, as this increases the mass flow of material to be deposited and therefore results in a larger molten pool, which is more prone to contamination [10].

In contrast, the travel speed of the torch is inversely proportional to the width and depth of the weld bead, i.e., its increase leads to a reduction in the width and depth of the welding bead since it also reduces the heat input [10].

The flow of the shielding gas and its mixture affect the morphology of the bead, the stability of the process and the transfer mode, but its main purpose is to ensure the stability of the electric arc and to protect the molten pool, which prevents them from reacting with the surrounding atmosphere, thus reducing undesirable phenomena such as oxidation. The shielding gas can either be inert, such as argon (Ar) or helium (He), or active, such as carbon dioxide (CO_2), and its selection depends primarily on the material to be deposited and the available budget. Furthermore, it is also necessary to consider the gas flow rate, since turbulent flow causes the gas to mix with the surrounding atmosphere, resulting in a defective protection and increasing the possibility of oxidation [11].

Therefore, for each equipment and material, it is essential to optimize the various process parameters. The correct selection of parameters affects the transfer mode, which determines the width, penetration and size of the welding bead as well as the surface waviness and deposition rate.

2.3.2 DEFECTS AND MICROSTRUCTURAL FEATURES

The common feature of all manufacturing processes is the occurrence of defects that, depending on their size, morphology and location, can affect the mechanical properties of a component and consequently compromise its performance. WAAM technology is no exception and presents some challenges that must be surpassed in order to make the process more feasible.

The fact that it has similar fundamentals to the conventional welding processes is an advantage since the formation of defects is equivalent in both cases, and there is an extensive knowledge about defect formation as well as active and/or passive techniques to prevent its formation in welding processes [2]. The most significant defects inherent to the WAAM process are described below.

RESIDUAL STRESS

This is the stress that remains in the part after all external loads have been removed. It is known as residual stress, and it is in equilibrium in a specific region of the material. This stress has an impact on the mechanical properties of the component, resulting in distortions that hinder the fulfilment of the required tolerances. During WAAM, high temperature gradients are achieved, which cause significant deformations, resulting in residual stress after the cooling process. This stress is only detrimental when it exceeds the yield strength of the material, resulting in plastic deformation, but if it exceeds the tensile strength it will cause the fracture of the material [5].

Residual stress can either be longitudinal or transverse and it occurs when the part is exposed to non-uniform temperature fields that promote successive expansion and contraction of the part [12]. Furthermore, the variation of the contact tip to work distance (CTWD) can affect the magnitude and distribution of residual stress in both the substrate and the beam [13].

There are several techniques to mitigate and/or reduce the formation of residual stress, such as optimizing the process parameters due to their influence on the part's thermal cycles. Mughal et al. [14] studied the influence of the deposition path on residual stress distribution. It was concluded that beginning the deposition from the outside of the workpiece and ending it in its center is the deposition strategy with the least influence on the formation of residual stress.

CRACKING AND DELAMINATION

Delamination is the separation of two consecutive layer and it is caused by the presence of residual stress at the interfaces of the layers, surpassing the yield strength of the material [1]. Furthermore, delamination can result from the insufficient re-melting of the previously deposited layer, causing a weak adhesion between layers. This kind of delamination can be avoided by adjusting the process parameters with the aim of increasing the heat input, thus ensuring a better bond between consecutive layers. That said, it is possible to increase the re-melting percentage of the preceding layer by pre-heating the substrate [2].

Similarly, cracking depends on the material used and process parameters. Nonetheless, the predominant factor is the composition of the deposited material, as the use of alloys composed of differing materials increases the susceptibility to crack formation due to the differences in their properties.

POROSITY

Porosity is a defect that can either be induced by the process or by the raw material. It has a negative impact on the mechanical properties of the material and so it must be mitigated. It is possible to control the presence of such defects through the proper usage of the shielding gas, selecting the most appropriate composition for the application and material involved.

One of the main causes of porosity formation is the absorption of atmospheric gases by the molten pool, such as oxygen, hydrogen and nitrogen. Particularly, the deposition of aluminum alloys is more susceptible to the formation of these defects due to the high solubility between hydrogen and aluminum in the liquid state. The aluminum's capacity to dilute the hydrogen is higher when the aluminum is in the liquid state and reduces drastically during solidification, which leads to the retention of hydrogen within the solid material, forming porosities [15].

The cleaning of the raw material is crucial to minimize porosity formation during deposition, since the presence of impurities in the wire feedstock and/or substrate can be absorbed by the melt pool, causing porosity and inclusions. Accordingly, Ryan et al. [16] investigated the influence of the surface finish of the metallic wire, travel speed and wire feed speed on the formation of porosities in the AA2319 aluminum alloy. It was found that the surface finish of the wire is the most important aspect in porosity formation as it affects the hydrogen content on the wire surface and the stability of the arc. Meanwhile, the process parameters WFS and TS and the composition of the wire showed a negligible influence on pore size reduction.

ANISOTROPY

During WAAM, the deposited material is submitted to successive heating and cooling cycles, resulting in different microstructures along the part that determine the material's mechanical properties. The typical microstructure of WAAM parts is composed of columnar grains that form because the solidification conditions of the material favor grain growth in a preferential direction, as there are fewer nucleation points at the solid/liquid interface [13]. This type of growth leads to anisotropic properties that can be detrimental in circumstances that involve loads in multiple directions.

It is therefore intended that the materials' microstructure in most applications feature equiaxed grains with no preferential orientation, as these can minimize the propensity for cracking while improving ductility, which results in components with isotropic properties [1]. There are several approaches for controlling the microstructure, such as heat treatments after deposition, by monitoring the part's cooling or introducing inoculants into the molten pool to refine the microstructure.

2.4 WAAM PROCESS VARIANTS

WAAM technology has received special attention and recognition from the industry due to the inherent advantages of the process. The high deposition rate allows to produce large components with reduced cost, shorter lead times and minimal material waste. Nevertheless, it is essential to overcome the limitations presented above to achieve the industrialization of the process. Some of the WAAM process variants are presented below, which aim to mitigate and/or eliminate the typical shortcomings of the process, organized into three types of approach: mechanical, thermal and chemical.

2.4.1 MECHANICAL APPROACH

Mechanical variants of the WAAM process have been developed with the aim of benefiting from the advantages inherent in plastic deformation, particularly grain refinement and the resulting reduction in the anisotropy that is typical of this process. These variants can be classified according to the temperature at which they are performed (hot or cold). Applying plastic deformation to the surface of the manufactured parts leads to other advantages, namely the reduction of surface waviness, which facilitates the performance of non-destructive testing (NDT) that involves direct contact with the part. This is a crucial aspect for the industrialization of AM processes [17].

Colegrove et al. [18] developed the high-pressure rolling technique, which is schematically represented in Figure 2.3. It consists of applying a load up to 100 kN on a roller that travels through the deposited layers, promoting plastic deformation in order to refine the microstructure, thus reducing grain size and improving the material's mechanical properties. The

plastic deformation occurs after the deposited layer has been cooled to room temperature and so it is categorised as a cold process.

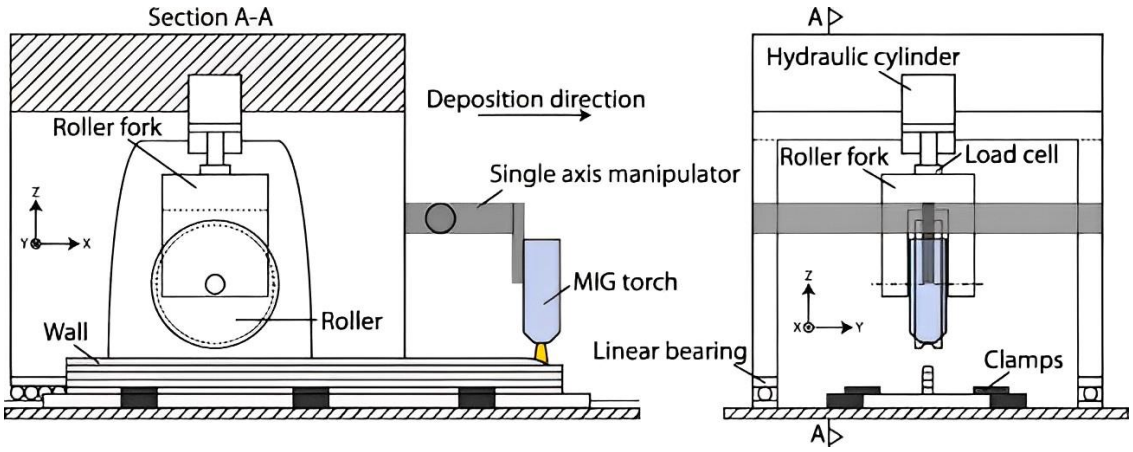

Figure 2.3 - Schematic representation of the high-pressure rolling technique [18]

This technique was tested by Martina et al. [19] for the titanium alloy Ti-6Al-4V. The performed tests demonstrated that applying the roller between layers induced a refinement of the β grains, a reduction in thickness of the α-phase lamellae, and a microstructure transformation from columnar to equiaxial. Additional studies have been conducted to achieve further benefits, particularly to control residual stress and distortion in aluminum [20] and titanium alloys [21].

Another advantage is the reduction of porosity, especially in the deposition of aluminum alloys, where the common presence of pores restricts their usage. Increasing the applied load on the roller makes it possible to reduce the number and size of pores, which has been identified as the main reason for the increased ductility in aluminum alloys [5]. Despite being an effective technique in reducing grain size and collapsing porosities, it requires a highly rigid system that can withstand high loads of up to 100 kN. Moreover, it is a time-consuming process as it is necessary to wait until the material has cooled to room temperature before applying the plastic deformation, thus making its industrialization unfeasible.

Later, Hönnige et al. [22] used a machine hammer peening (MHP) technique with the intention of improving the flexibility and speed of the previous method. This variant applies plastic deformation to the upper surface of a set of four consecutive layers and to the lateral surface of the manufactured part. The tests conducted on the Ti-6Al-4V titanium alloy revealed that by applying this technique between the deposition of each layer, it is possible to refine grain and improve the material's mechanical properties. Grain refinement can also improve fatigue resistance and reduce the risk of crack growth [23].

The variants that use cold plastic deformation can significantly reduce residual stress and distortion, increase microstructural homogeneity, improve the mechanical properties and reduce porosity. However, equipment with high structural rigidity is required to support heavy loads, which are necessary for cold plastic deformation. Additionally, their use can extend the lead time, thereby devaluing one of the most important features of the WAAM process, which is the high deposition rate [5].

This prompted the need to study new techniques that apply hot plastic deformation in order to reduce the applied loads. Zhang et al. [24] created the hot micro-rolling variant, where the roller accompanies the torch movement from a constant distance, deforming the material at temperatures above 800 ºC between the deposition of each layer. This technique has shown improvements in the dimensional accuracy and mechanical properties of the manufactured parts. However, this method still entails the production of specific equipment with high structural rigidity, which prevents the use of conventional XYZ tables or robotic arms. This increases the cost associated with the process, making it less competitive [25].

With the aim of reducing the applied loads and avoiding the waiting time for material cooling between the deposition of each layer, Duarte et al. [25] developed the hot forging variant (HF-WAAM), which uses a hammer placed inside the shielding gas nozzle to perform hot forging on the deposited material, as illustrated in Figure 2.4. Similar to the conventional hot forging process, this forging occurs at temperatures close to 900 ºC, exceeding the material's recrystallisation temperature.

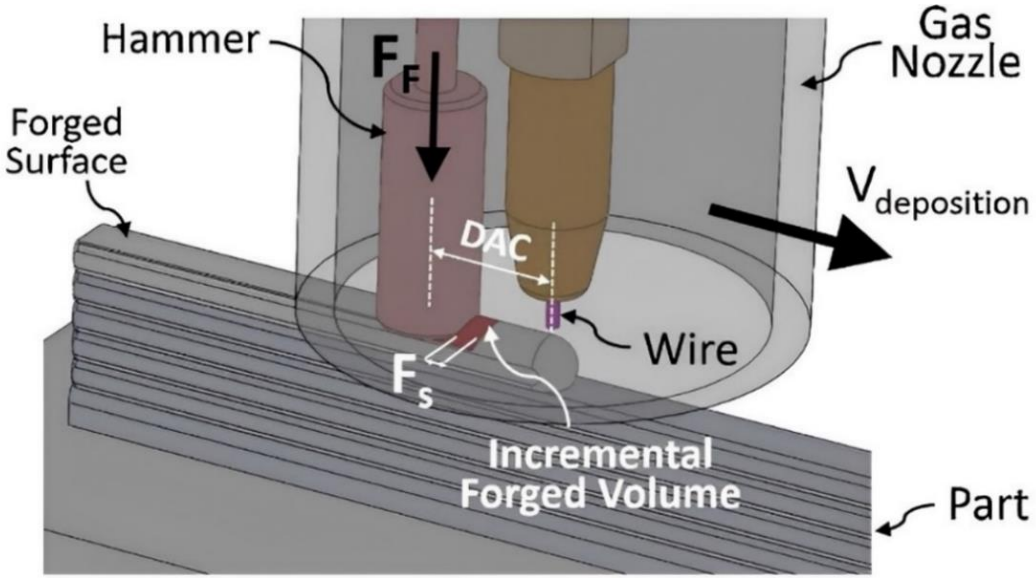

Figure 2.4 - Schematic illustration of HF-WAAM [25]

The main goal was to cause the plastic deformation of the material at high temperatures in order to reduce residual stress, collapse porosities, eliminate the need for heat treatment operations and homogenize the microstructure. The experiments carried out on the AISI316L stainless steel revealed an improvement in the material's mechanical properties due to the increase in the yield strength and tensile strength. This is due to the fact that hot forging promotes a reduction in grain size, increasing the amount of grain boundaries and, consequently, improving the material's mechanical strength. However, there is a reduction in the material's ductility, which represents the ability to deform plastically until fracture. Nevertheless, this reduction is insignificant for this material and does not compromise its performance in most industrial applications. These results are represented in Figure 2.5.

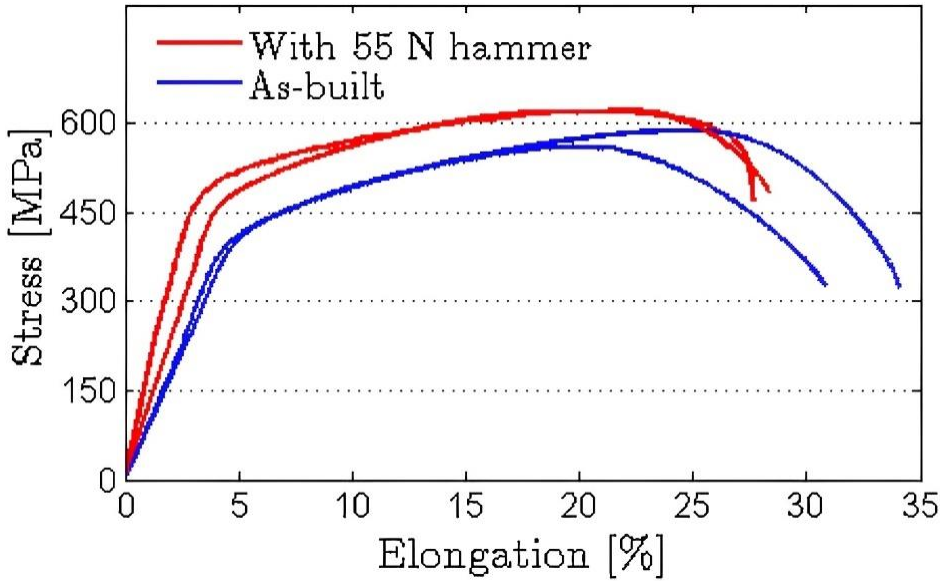

Figure 2.5 - Uniaxial tensile stress-strain curves for WAAM (as-built) and HF-WAAM (with 55 N hammer) samples [25]

In order to test the influence of this technique on pore collapsing, samples were manufactured without the use of a shielding gas to promote pore formation. It was found that there was a decrease in the size and number of pores and that they shifted to a more peripheral region. It was also observed that increasing the forging load changes the shape of the pores from spherical to oval. Moreover, it was verified that for a load of 55 N and using a parallelepiped hammer, some of the pores were fully collapsed, as can be seen in Figure 2.6.

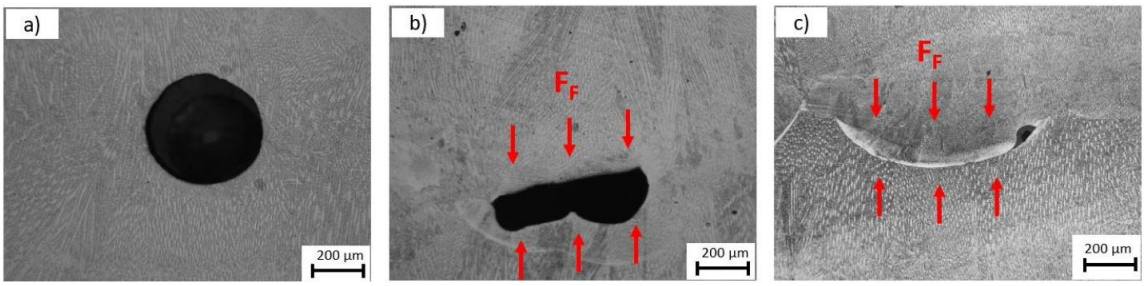

Figure 2.6 - Porosity analysis in samples produced with HF-WAAM without shielding gas with a load of: a) 17 N; b) 55 N; c) 55 N with reduced area [25]

Furthermore, it was observed by the authors that the use of this technique results in a more homogeneous and isotropic microstructure, with a smaller grain size and no texture. The tests conducted on the CuAl8 alloy revealed that the samples manufactured with the conventional WAAM process have a significant variation in the yield stress and tensile strength values for different orientations. Meanwhile, when using the hot forging technique, there is a significant reduction in the variation of yield strength and tensile strength values, resulting in more isotropic properties. Moreover, this technique has been proven to reduce and homogenize the residual stress in the obtained parts [26].

Besides the substantial improvements in the material's mechanical properties, there is an advantage associated with the application of non-destructive testing. The hot forging causes a flat surface that facilitates the coupling of probes that can perform NDT, such as ultrasounds or eddy current tests, reducing the need for post-processing operations.

The study of this variant involved forging loads between 17 and 55 N, which are considerably lower than the forces required in the previously presented variants. Therefore, it can be concluded that the HF-WAAM technique offers a competitive advantage over the others, since it does not require equipment with high structural rigidity and can be implemented on conventional XYZ moving tables or robotic arms with 6 degrees of freedom. Furthermore, since the forging forces are fairly low, there is a reduction in the energy consumed during the process and less wear and tear on the equipment and tools used. Lastly, the fact that it is not necessary to wait for the material to cool means that it can be used without increasing the production time.

2.4.2 THERMAL APPROACH

One of the key characteristics for determining the properties of the final part is the interlayer temperature, i.e., the temperature of the previously deposited layer immediately before the subsequent layer is deposited. This characteristic dictates the conditions for heat dissipation by conduction through the part, affecting the cooling rate and thus affecting the microstructure and mechanical properties of the part. High interlayer temperature combined with high heat input leads to a lower heat dissipation and thus to a reduced cooling rate, which results in a coarse microstructure and can cause anisotropic properties in the material [2].

The difficulty in reducing heat accumulation makes it harder to maintain a low interlayer temperature. Although a high interlayer temperature increases the wettability of the molten metal, it can also cause an unstable deposition [27]. Furthermore, the time required to cool the part to a favorable temperature may lead to an unfeasible production time with extensive dwell time. Montevecchi et al. [28] developed a technique based on the finite element method to simulate the thermal behavior during the part's production, which makes it possible to both optimize the waiting time and monitor the interlayer temperature. However, in order to achieve the same interlayer temperature in each deposition, the dwell time must be increased until around the 21st layer. This leads to an increased production time and thus some researchers have been addressing this issue by using forced cooling techniques.

One of the forced cooling techniques involves the application of a gas jet immediately after the electric arc, which can be applied simultaneously with the deposition or between the deposition of each layer. The used gas can either be dry air [29] or CO_2 [30]. The tests undertaken have highlighted the potential of this technique in reducing surface oxidation, refining the microstructure and improving mechanical properties, since more effective heat dissipation increases the material's cooling rate. Moreover, the fact that cooling can be applied simultaneously with the deposition reduces the dwell time and therefore increases productivity.

A different variant of forced cooling consists of submerging the workpiece in a water tank, whose water level rises as the layers are deposited. Figure 2.7 illustrates the experimental setup used for this technique. The results demonstrated that it is possible to refine the microstructure and reduce the anisotropy of the obtained parts. Additionally, the influence of water on porosity formation was evaluated due to the presence of hydrogen in its composition, which could contaminate the molten pool. It was concluded that the use of water in this variant does not lead to an increase in pore volume [31].

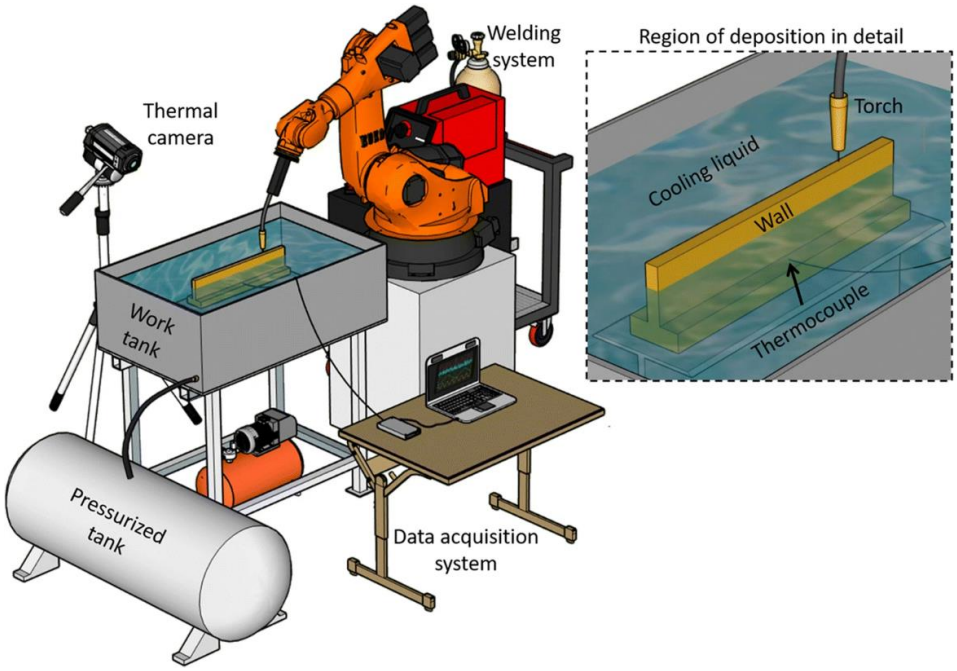

Figure 2.7 - Schematic representation of the experimental setup using a water tank [31]

The drawback of techniques that promote higher cooling rates of the components is their greater susceptibility to causing higher residual stress. One of the most common methods for minimizing cracking and residual stress is to preheat the substrate to reduce the thermal gradients and homogenize the temperature distribution.

Bai et al. [32] have developed a technique to reduce residual stress. It consists of an inductor with two identical coils attached to both sides of the workpiece, as shown in Figure 2.8. The inductor can perform both pre-heating and post-heating, depending on its relative positioning to the electric arc.

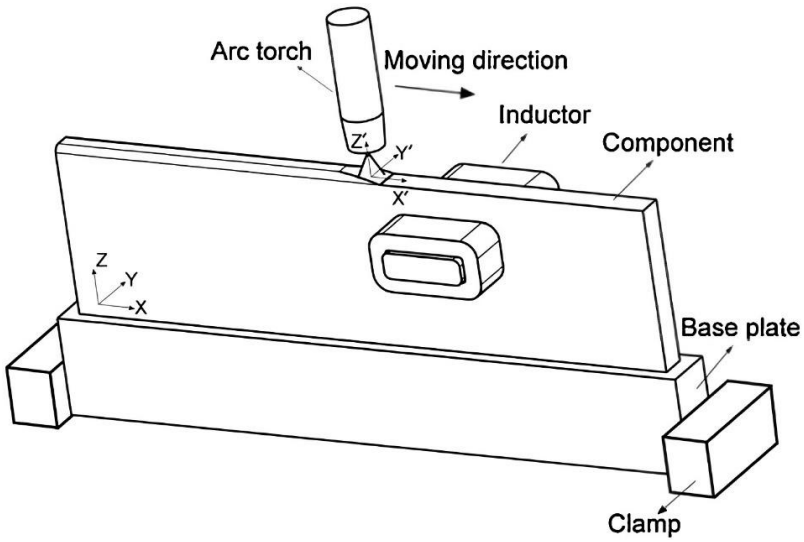

Figure 2.8 - Schematic illustration of the technique that uses an inductor [32]

The effect of various induction heating strategies on residual stress and temperature was studied through the finite element method. It was found that both pre-heating and post-heating led to a reduction in the residual stress, since both reduced the material's cooling rate. Nonetheless, the pre-heating technique proved to be more efficient since it induces a prior volumetric expansion of the material and lowers its yield strength.

2.4.3 CHEMICAL APPROACH

It is also possible to control the part's microstructure through the introduction of particles that have a higher melting point than the material being deposited. These particles are known as inoculants and their addition creates additional nucleation points, resulting in a finer and more homogeneous microstructure. The most common techniques involve adding them directly to the molten pool.

Some literature works have been developed in this direction, for example by adding silicon carbide (SiC) particles in-situ during the deposition of a high-strength low-alloy steel (HSLA) or by adding TiN particles during the deposition of a titanium alloy through the conventional WAAM deposition process. The results reveal a refined microstructure and, as a result, an improvement in the mechanical properties of the material as well as a reduction in the anisotropy that is typical of WAAM parts [33,34].

2.5 MATERIALS

Typically, most of the materials available in the form of welding wire can be used in WAAM. However, the most used materials are steel, aluminum, titanium and nickel alloys.

Previously, it was emphasized how important it is to monitor the cooling rate of the material during manufacturing. The heat dissipation conditions determine the microstructure, mechanical properties and surface waviness of the obtained part [30,35]. There are some helpful tools for predicting the microstructure and the resulting properties of materials, particularly the iron-carbon diagram, shown in Figure 2.9. This diagram is a graphical representation of the microstructural phases of iron and carbon, which depend on temperature and carbon content, with the main phases being austenite, ferrite and cementite.

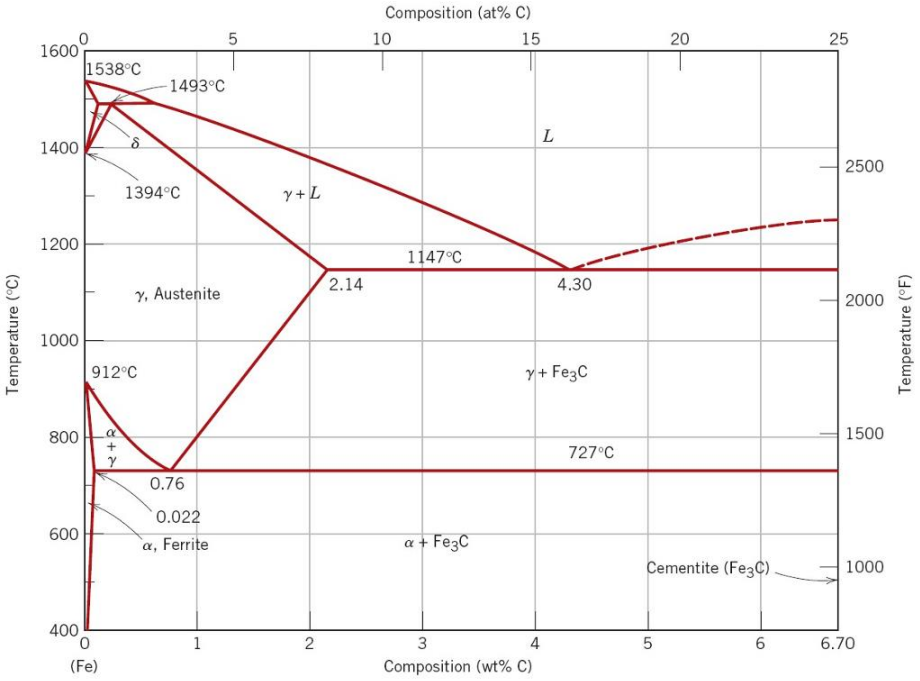

Figure 2.9 - Iron-carbon diagram (Adapted from [36])

Simultaneously, a continuous cooling transformation (CCT) phase diagram is used, which is represented by curves that show the cooling rate as a function of time and temperature. As a result, it is possible to identify the type of phase that will be formed in each point of the graph. Each phase confers distinct properties to the material and its choice depends on the application concerned. Figure 2.10 displays the CCT diagram for an HSLA steel.

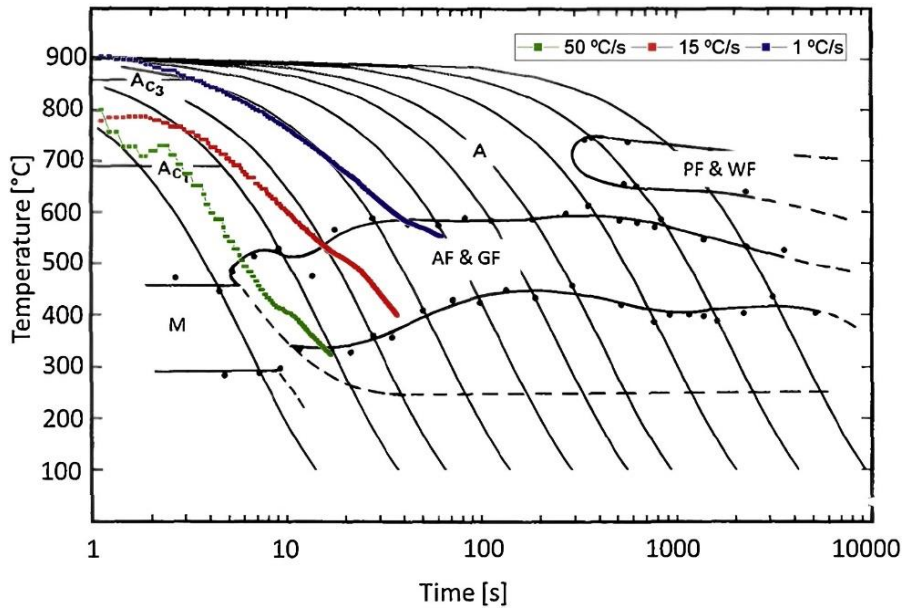

Figure 2.10 - CCT diagram for a HSLA steel with overlapping of experimental cooling rate curves (Adapted from [37])

It can be seen that cooling rates greater than 100 ºC/s lead to martensite formation which, in turn, causes an increase in the yield and tensile strength, with the downside of reducing ductility. Meanwhile, a lower cooling rate leads to grain growth and to a microstructure mostly composed of ferrite, which can cause anisotropic properties in the component. Its advantage is the capacity to reduce thermal distortion and residual stress.

Therefore, it can be concluded that combining both these diagrams helps to optimize the material's cooling process according to its microstructure. Thus, monitoring the cooling rates can enable the production of components with customized microstructures and properties for each application.

3 EXPERIMENTAL PROCEDURE

Part of this work was the design of a new HF-WAAM hammer capable of cooling the workpiece. The main modification was the addition of 2 slots that function as cooling channels.

3.1 DESIGN AND MANUFACTURE OF THE COOLING DEVICE

The cooling hammer design involved some modifications to incorporate cooling functionality. Two slots were strategically added to act as dedicated cooling channels. These channels were designed to optimize the flow and distribution of coolant throughout the part. In this way, it is possible to optimize heat dissipation, avoiding an excessive increase in the temperature of the workpiece.

To enable the coolant flow, two holes were made in each channel, designated for the inlet and outlet of the cooling channel. The inlet is located at a lower level than the outlet to facilitate the efficient circulation of the coolant, since hot fluid tends to rise due to its lower density compared to cooler fluid. In each of these four holes, M nuts were brazed to allow the later integration of connectors (RS Pro Swivel Male Elbow - BSPT 8-1/8) and tubes through which the liquid circulates. Between each connector and the respective tube, a thermocouple type N capable of measuring the temperature at the inlet or the outlet of each channel was inserted.

A Thermoplastic Polyurethane (TPU) gasket was manufactured using the Fused Deposition Modelling (FDM) 3D printing process to prevent the coolant from leaking through the top of the hammer. The printer model used was the Original Prusa i3 MK3S. This essential addition ensures the integrity of the cooling system, maintaining the desired cooling effect on the hammer throughout the process.

The hammer that was conceived specifically for this project is displayed in Figure 3.1, where the geometry and shape of both cooling channels can be seen. A dual counter-flow cooling system was chosen as it promotes a higher heat homogenization and transfer rate, thus allowing for a greater removal of thermal energy.

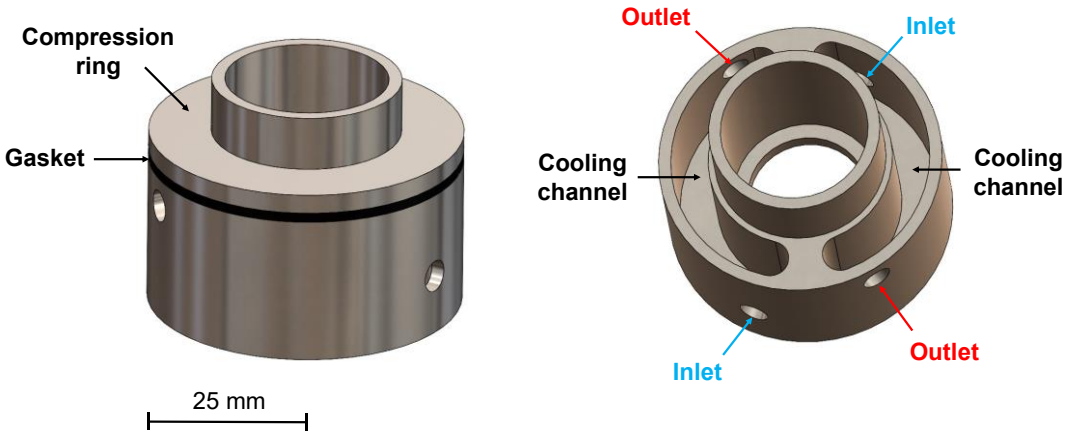

Figure 3.1 - Geometry and shape of the developed cooling hammer

3.2 MATERIALS AND METHODS

A commercial high-strength low-alloy (HSLA) steel AWS A5.28 ER110S-G wire electrode with a diameter of 1 mm was used as the feedstock material. The selection of this material was based on the fact that the HSLA undergoes transformations in the solid state, which makes it easier to change its properties by heat treatments, though it is a hardenable steel. Table 3.1 and Table 3.2 show, respectively, the chemical composition and mechanical properties of the deposited wire.

Table 3.1 - Chemical composition of ER110S-G wire (wt%) [38]

C	Mn	Si	Ni	Cr	Mo	V	Cu
0.08	1.70	0.44	1.35	0.23	0.30	0.08	0.25

Table 3.2 - Mechanical properties of as-deposited material with ER110S-G wire [38]

Yield strength (MPa)	Tensile strength (MPa)	Elongation (%)	Impact ISO-V - 40°C (J)	Hardness (HV)
710	790	20	70	295

Regarding the cooling system, the coolant used was the antifreeze G13, with a freezing point of -37 ºC. This is a glycerin-based liquid, which has a lower environmental impact when compared with glycol based liquids. For the circulation of this fluid, it was used a closed system in which the tank has a capacity of 40 L, thus functioning as a thermal mass. In order to maintain the low temperature of the fluid while circulating in the system, the tank was placed in a freezer with the capacity to reach a temperature of approximately -25 ºC. Two pumps with a flow rate of

1.8 kg/min each, were used to pump the coolant from the tank to the hammer. Each pump was separately connected to one of the hammer channels. Figure 3.2 shows the details of the deposition system and temperature acquisition system using thermocouples.

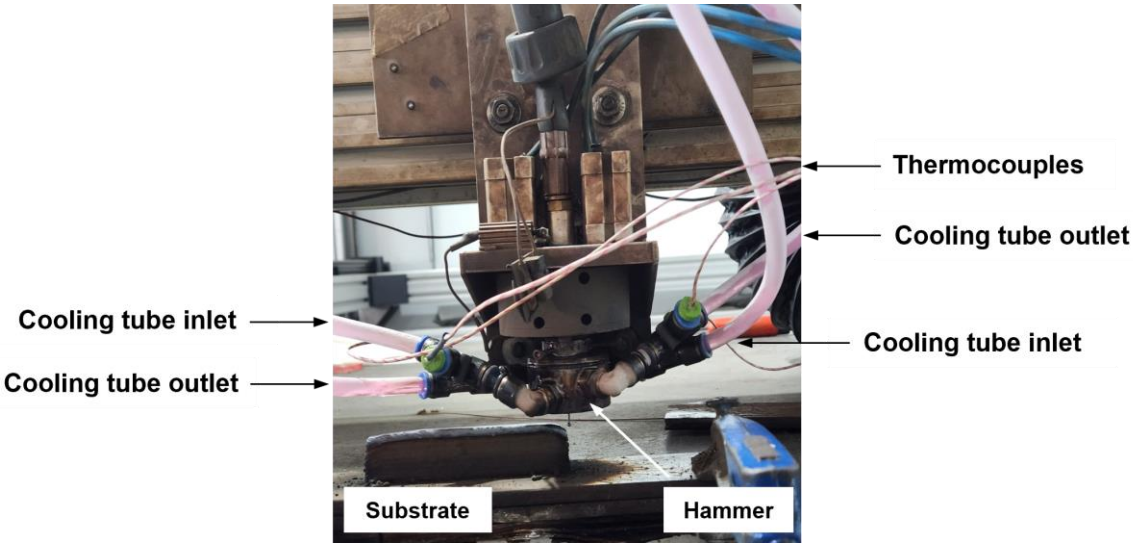

Figure 3.2 - Details of the deposition system and temperature acquisition system using thermocouples

The cooling system was designed with the aim of cooling the hammer that is used in HF-WAAM and that can be simultaneously used in conventional WAAM as a thermal mass that cools the surrounding environment of the molten pool. Thus, to evaluate the effect of the developed cooling system, WAAM and HF-WAAM samples were manufactured, with and without hammer cooling. The experimental setup scheme is represented in Figure 3.3.

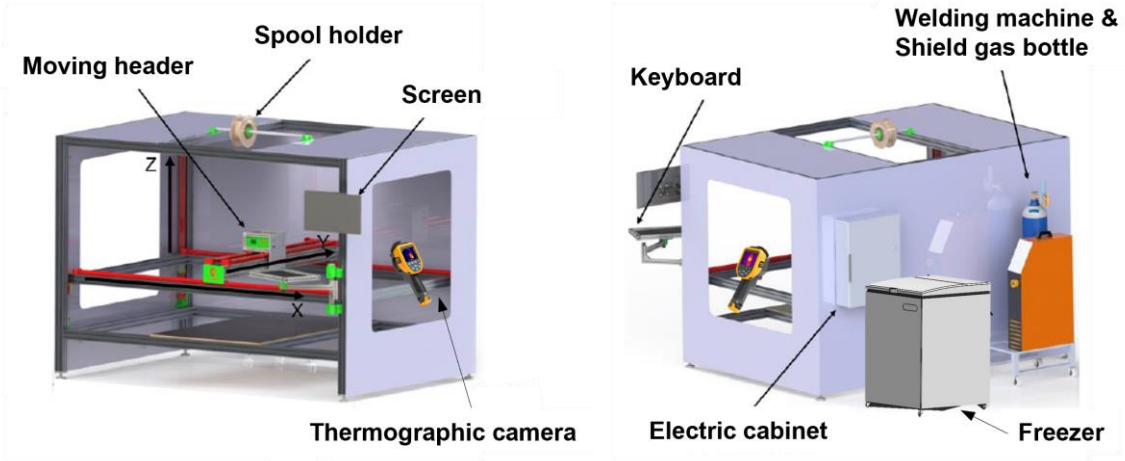

Figure 3.3 - Schematic representation of the experimental setup [2]

A customized WAAM torch was attached to a 3-axis CNC machine in a working space of 2760 x 1960 x 2000 mm. An Oerlikon welding machine with a CITOWAVE III 520 power source, a DMU W500 control unit and a wire feeder was used to deposit the material onto a mild steel substrate (300 x 60 x 8 mm). The details of the developed and patented torch are depicted in Figure 3.4, where the hammer used to perform the in-situ interlayer hot forging can be observed. The hammer is actuated by two pneumatic actuators (Festo ADN-12-10-I-P-A) symmetrically positioned to prevent any discrepancies in the generated forces.

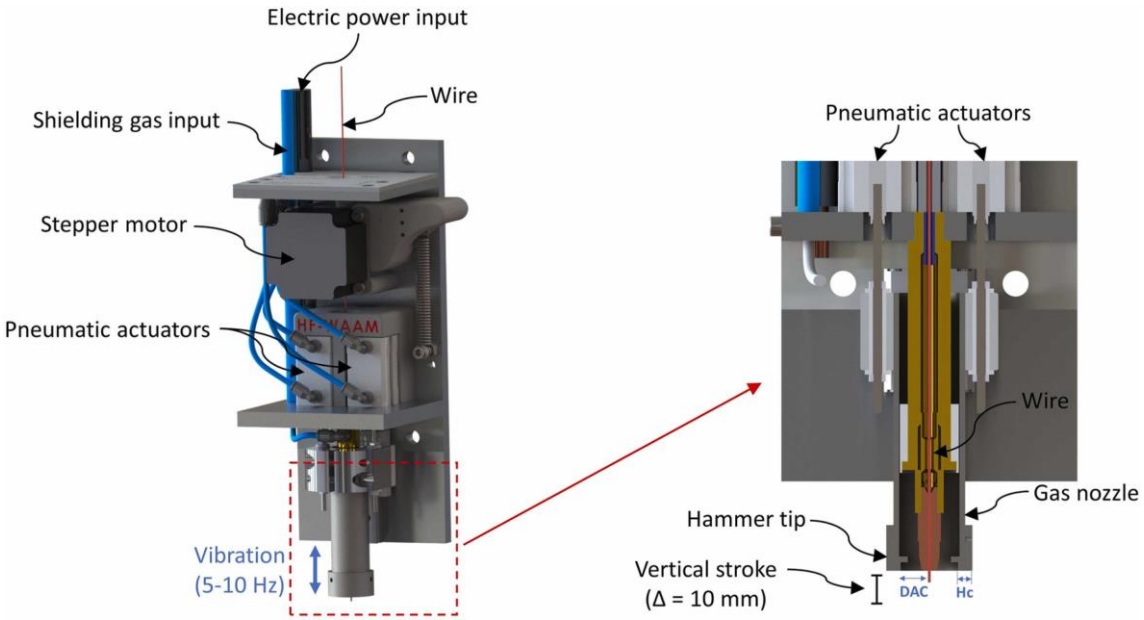

Figure 3.4 - Schematic representation of the developed torch for in-situ Hot Forging WAAM (HF-WAAM) [26]

During deposition, a Fluke TI400 thermographic infrared camera was used to monitor the temperature of both sample and hammer throughout deposition. The camera had a resolution of 320 x 240 pixels, a wavelength range of 7.5 - 14 µm, an accuracy of ± 2%, a measurement range of -20 to +1200 ºC and a refresh rate of 9 Hz. The emissivity was set to 0.84, taking into consideration the available literature [39]. Videos were recorded capturing the entire deposition process and the SmartView software was used to process the data retrieved at different points of each deposited layer. This data was then analyzed to calculate the material thermal cycles during deposition as well as the hammer temperature throughout the entire process.

Nonetheless, given that the metal fuses at temperatures around 1200 ºC and the material emissivity changes with the temperature, there is some uncertainty attached to the absolute values obtained, however, a relative comparison can be made since the manufacturing of all samples followed the same methodology.

3.3 PROCESS PARAMETERS

The shielding gas used was the ARCAL™ Force (Ar 82%, CO_2 18%) and the deposition strategy was Zig-Zag, i.e., consecutive layers were deposited in alternate directions, resulting in a more uniform distribution of residual stresses, thus avoiding a height disparity within the part. The remaining process parameters used to produce the samples are presented in Table 3.3, where it is observed that samples 1 and 2 were obtained by conventional WAAM whereas samples 3 to 6 used the interlayer hot forging previously presented (HF-WAAM). Aiming to evaluate the capability of the hammer to remove heat from the part during contact, samples 3 and 4 were forged with a 20% duty cycle, i.e., during each cycle the hammer was in contact with the deposit for 20% of the time and in the air for 80% of the time. Meanwhile, samples 5 and 6 were forged with an 80% duty cycle, where the hammer remained in contact with the workpiece for 80% of the time. These samples were manufactured with 21 layers over a length of 120 mm to perform the microhardness and metallographic tests. Subsequently, another four samples were produced with 40 layers over a length of 160 mm, utilizing the parameters of samples 1 (WAAM), 2 (WAAM-C), 5 (HF80) and 6 (HF80-C), which were then used to perform the mechanical tests.

As can be verified from Table 3.3, samples 2, 4 and 6 were fabricated with the cooling system on. Since sample 2 was not forged, its cooling occurred only through the proximity of the hammer to the workpiece, thus functioning as a cooled surrounding mass, instead of direct contact, as was the case with samples 4 and 6.

Table 3.3 - Process parameters used for sample deposition

	WAAM		HF-WAAM			
	Sample 1 **WAAM**	Sample 2 **WAAM-C**	Sample 3 **HF20**	Sample 4 **HF20-C**	Sample 5 **HF80**	Sample 6 **HF80-C**
Welding Mode	MIG welding (DC+)					
WFS (m/min)	4					
TS (m/min)	0.36					
Voltage RMS (V)	18					
Current RMS (A)	123					
Gas flow rate (L/min)	18					
Interlayer temperature (ºC)	150					
CTWD (mm)	14					
Forging frequency (Hz)	-		7 Hz			
Duty cycle (%)	-		20		80	
Cooling system	-	G13	-	G13	-	G13

CTWD – Contact tip to work distance

3.4 HEAT INPUT CALCULATION

Within the scope of arc welding processes, heat input (HI) is a crucial measurement of the amount of energy transferred from the arc to the workpiece. It is expressed in energy per unit of length (J/mm) and it's calculated according to Equation (3.*1*.

$$HI = \frac{U \times I}{TS} \cdot \eta \tag{3.1}$$

Where U (V) is the Root Mean Square (RMS) of the voltage, I (A) is the RMS of the current, TS (mm/s) is the travel speed of the torch and η is the efficiency of the welding process, considered to be 80% for arc welding.

3.5 CHARACTERIZATION TECHNIQUES

3.5.1 METALLOGRAPHIC ANALYSIS

A metallographic analysis was carried out to assess potential changes in the macro and microstructure along the height of the samples, i.e., both the middle and top of the parts were analyzed and compared. Moreover, it was possible to analyze grain size and identify eventual defects as well as their morphology. For this analysis a Leica DMI 5000 M inverted optical microscope was used. Cross section samples were taken from the middle region of the total length of the deposited walls in order to investigate the correlation between microstructural evolution and mechanical properties in the built walls. The samples were grinded and polished with a 1 µm abrasive diamond paste, followed by a chemical attack with a 3% Nital solution to facilitate microscopic analysis.

To complement the experimental approach and assist in analyzing the results, the continuous cooling transformation (CCT) diagram of the HSLA steel was simulated using the commercial software JMatPro. The input data was the chemical composition of the feedstock material (Table 3.1) and an austenitisation temperature of 900 °C was considered. Moreover, the grain size of prior austenite was varied between 10, 25, 50, 100, 500 and 1000 µm in order to assess the effect of hot forging on the material's hardenability. The main purpose is to demonstrate the effect of these factors on the expected microstructure and to simulate different regions of the material under multiple thermal cycles.

3.5.2 MICROHARDNESS TESTING

After analyzing the samples through optical microscopy, microhardness measurements were carried out. For this test a Mitutoyo HM-112 Micro-Vickers Hardness Tester was used, applying a test load of 4.9 N for 10 s. The measurements were performed from the substrate along a vertical line in the middle of the sample’s cross-section, with a distance of 0.5 mm between each indentation, allowing a detailed analysis of the hardness profile.

3.5.3 ELECTRICAL CONDUCTIVITY MEASUREMENTS

To complement the previous techniques, the electrical conductivity field of the manufactured parts was measured through eddy currents. The four-point potential drop measurement technique was used to assess changes in the electrical conductivity of the processed materials compared to the non-affected substrate. A standard Jandel™ four-point linear probe with a probe tip radius of 40 µm and a probe spacing of 0.635 mm was used along with a Keithley 2182A nanovoltmeter. The experiments were carried out under a direct current of 80 mA. Moreover, a dedicated probe positioning system was used to guarantee the accurate positioning of the probe.

3.5.4 UNIAXIAL TENSILE TESTING

The first and last 20 mm of each sample were removed in order to avoid the regions that are most susceptible to the formation of defects, as the process is slightly unstable at the beginning and end of deposition. Afterwards, three transverse specimens and six longitudinal ones, whose dimensions are shown in Figure 3.5 a), were extracted from specific zones of each sample, as illustrated in Figure 3.5 b). The purpose of obtaining specimens from different areas is to assess the variation of mechanical properties along the sample. After being deposited, the parts were face-milled on a conventional flat grinding machine to ensure surface finishing and a uniform specimen thickness of 0.5 mm. Subsequently, the specimen profile was machined on a HAAS Super Mini Mill 2 machining center.

The uniaxial tensile tests were conducted on an Autograph Shimadzu model AG500Kng equipped with a Shimadzu SFL-50kN AG load cell with a total capacity of 50 kN. These tests were performed at room temperature and a displacement speed of 0.017 mm/s was applied. The data acquired from the tests is crucial for evaluating the Ultimate Tensile Strength (UTS), yield strength and the elongation to fracture values, which indicates the ductility of the material. The manufacturing of the specimens and the determination of their mechanical properties complied with the recommendations of ISO 6892-1:2019.

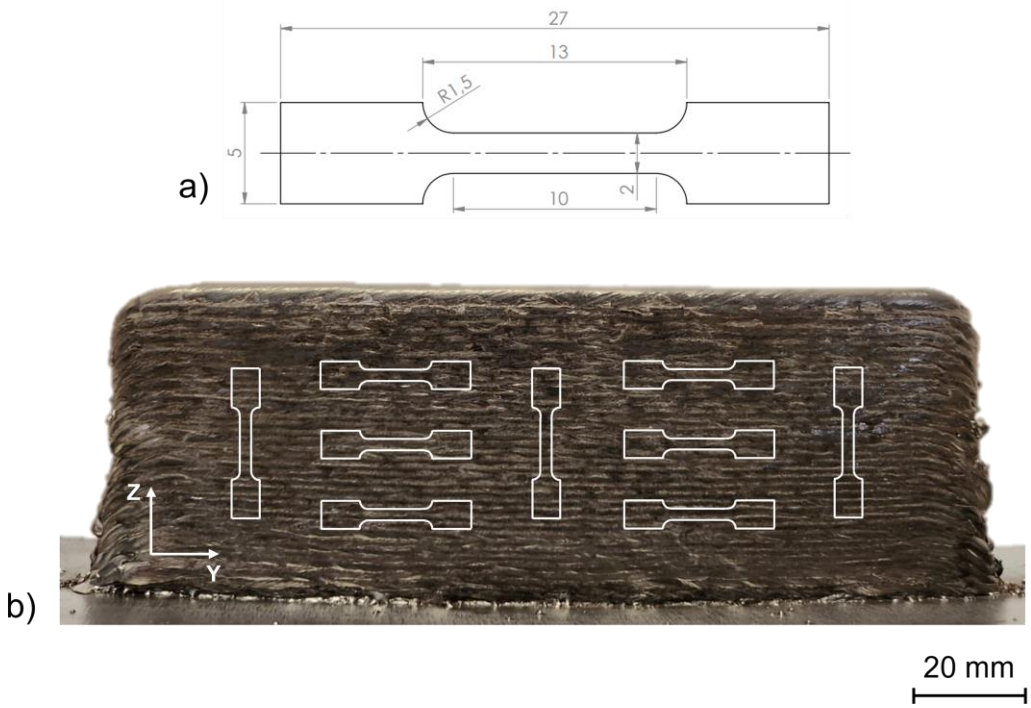

Figure 3.5 - Uniaxial tensile test specimens: a) dimensions (Adapted from [40]); b) removal location

After completing the uniaxial tensile tests, the ultimate tensile stress anisotropy was calculated for each sample according to Equation (3.*2*. Where A (%) is the percentage of anisotropy, UTS_{max} (MPa) is the maximum UTS value between longitudinal and transverse average results and UTS_{min} (MPa) is the minimum value.

$$A = \frac{UTS_{max} - UTS_{min}}{UTS_{max}} \cdot 100 \tag{3.2}$$

3.5.5 SCANNING ELECTRON MICROSCOPY

A Hitachi SU3800 Scanning Electron Microscope (SEM) with the acceleration voltage set to 20 kV was used to analyze the fracture surfaces of the specimens that were extracted from the samples manufactured under the various conditions and which were subsequently subjected to the uniaxial tensile testing.

4 RESULTS AND DISCUSSION

4.1 MACROSCOPIC CHARACTERIZATION

The set of samples obtained after the deposition of 21 consecutive layers for the metallographic analysis, microhardness and electrical conductivity tests was also characterized macroscopically. Figure 4.1 displays the visual aspect of the six produced samples. It can be seen that using the cooling system has contributed to a slightly improvement in the samples waviness and consistency of the deposited beads. Moreover, the hot forging has helped to homogenize the height of each layer, notably for the last deposited layer.

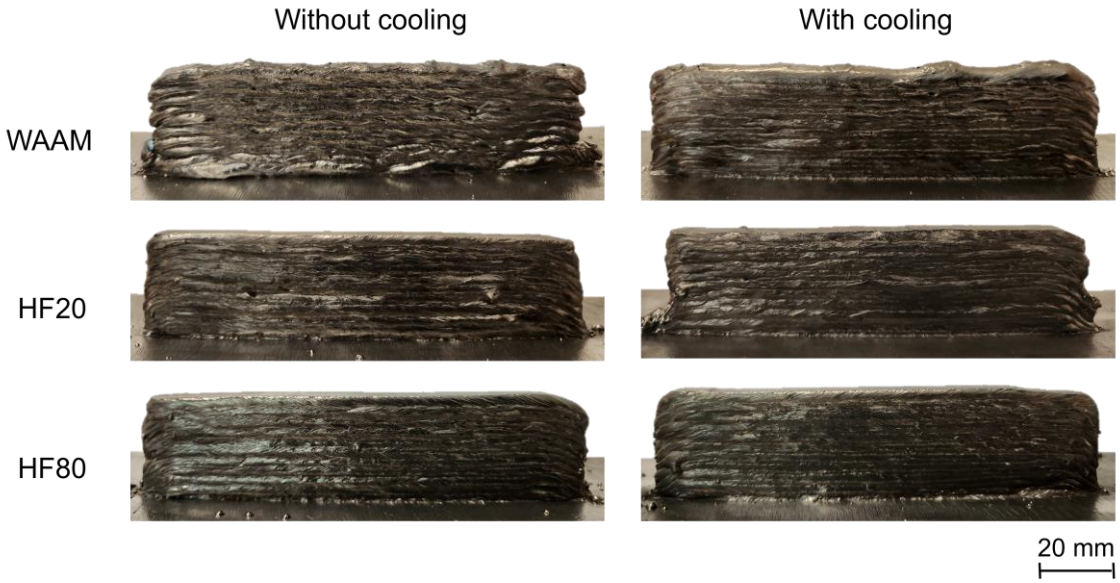

Figure 4.1 - Overall aspect of the parts manufactured under different conditions

Seven measurements of the height and width of each sample were taken over their 120 mm length with a 15 mm distance between each measurement. Table 4.1 presents these results. It is known that for higher walls, hot forging considerably changes its geometry, increasing the width and reducing the height. However, for a height of around 30 mm, the deformation caused by forging is small and does not cause a significant widening, i.e., the subsequent layers are not affected and the height of the wall does not decrease. Furthermore, it can be seen that there is a lower variation in the height and width of the samples manufactured with forging compared to the samples obtained through the conventional deposition process.

Table 4.1 - Height and width measurements for each sample

Sample Reference	**Height (mm)** $\mu \pm \sigma$	**Width (mm)** $\mu \pm \sigma$
WAAM	28.58 ± 1.26	7.40 ± 0.40
WAAM-C	29.40 ± 0.46	7.21 ± 0.14
HF20	27.65 ± 0.38	7.70 ± 0.29
HF20-C	28.33 ± 0.58	7.75 ± 0.38
HF80	28.37 ± 0.55	7.33 ± 0.26
HF80-C	29.29 ± 0.44	6.79 ± 0.24

4.2 THERMAL ANALYSIS

Heat dissipation during deposition is a crucial factor in determining the microstructure and mechanical properties of the deposited material. It can be achieved by the mechanisms of conduction, convection and/or irradiation. However, as the number of deposited layers increases, the efficiency of cooling by conduction diminishes due to the substantial area of substrate that facilitates heat dissipation in the first layers. Since the majority of the solid-state transformations take place between 800 and 500 °C, it is necessary to control heat transfer between subsequent layers, thereby influencing cooling rates and thermal cycles in order to achieve the intended microstructure and mechanical properties. Thus, the scope of this work was to evaluate the impact of cooling the hammer on the thermal cycles experienced by the workpieces during their deposition.

To broadly evaluate the material's cooling rate evolution during the deposition process, the temperature of the entire workpiece was monitored. Thus, it is possible to analyze the temperature variation in both time and space, which in turn points to the resultant microstructure, thereby optimizing the process for specific applications. Figure 4.2 reveals the thermal imaging obtained 3 s after the arc extinction of the last deposited layer (21st) for all the produced samples.

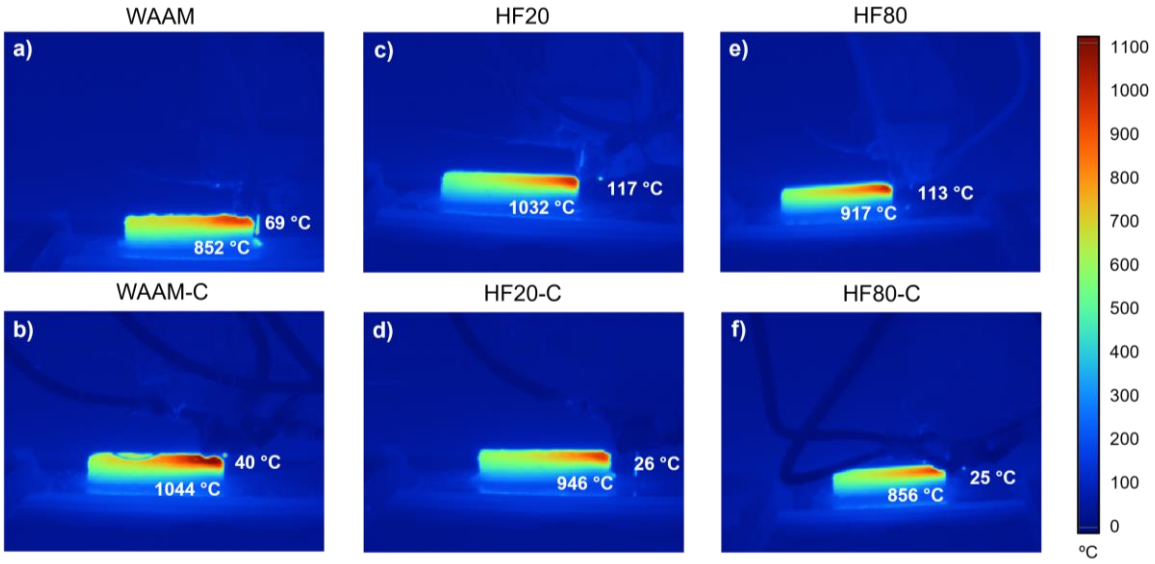

Figure 4.2 - Thermal imaging obtained 3 s after the arc extinction of the 21st layer of sample: a) WAAM; b) WAAM-C; c) HF20; d) HF20-C; e) HF80; f) HF80-C

Analyzing these thermographic images, it is possible to validate the effect of the cooling system on the hammer during deposition. It can be observed that during hot forging, the use of the cooling system lowered the average temperature of the hammer by 90 °C, which represents a 77% reduction. Additionally, it is shown that the duty cycle parameter does not have any influence on the hammer temperature due to the high temperatures achieved during deposition. However, regarding the highest temperature of the part, registered 3 s after the arc extinction of the 21st layer, it was verified that the use of the cooling system reduced this temperature by 8 %, in the parts manufactured with hot forging and that by increasing the duty cycle from 20 to 80 % the part's maximum temperature decreased form 946 °C to 856 °C. These findings were similar for the remaining layers.

The variation of the hammer temperature measured immediately after the arc extinction in each layer is represented in Figure 4.3. It can be seen that in samples produced by WAAM, the temperature stabilizes after the 4th layer at 70 ºC for the one obtained without cooling and at 35 ºC for the one obtained with cooling. In turn, in samples manufactured with forging, the hammer temperature is higher and stabilized at 115 ºC and only after the 5th layer for that obtained without cooling and at 25 ºC and after the 2nd layer for that obtained with cooling. Therefore, it can be concluded that the developed cooling system is effective in cooling the hammer even during the forging operation.

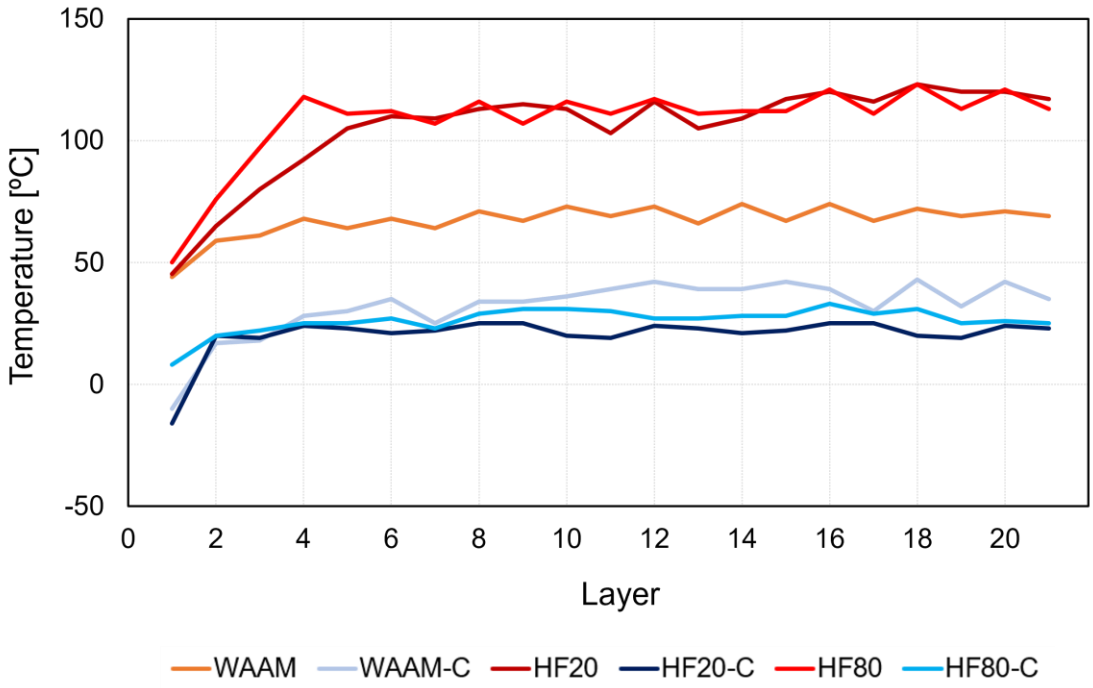

Figure 4.3 - Hammer temperature after the arc extinction of each layer of all produced samples

When comparing the difference between the temperature of the hammer and the temperature of the material being forged (1000~1200 ºC), there was a difference of around 885 °C for the part manufactured without the cooling system and 975 °C for the part manufactured with cooling. Therefore, the use of the cooling system caused a 9% increase in the difference between the hammer temperature and the material temperature.

Subsequently, the thermal cycles of the 7th layer were analyzed for all the samples in order to determine the cooling rates of the material between 800 and 500 ºC. Figure 4.4 illustrates these thermal cycles as well as the part's cooling rates, where each peak corresponds to the deposition of one layer. Some of the subsequently deposited layers did not generate sufficient energy to heat the 7th layer within this 800-500 ºC interval. In such cases and where the data was not consistent, no cooling rate was calculated. As was described in the methodology chapter, the WAAM-C sample was refrigerated by a cooled surrounding mass, where the coolant was pumped through the hammer channels, which remained above the part being manufactured and accompanied the welding torch, meaning that there was no contact between the hammer and the part, as occurred in the samples subjected to forging.

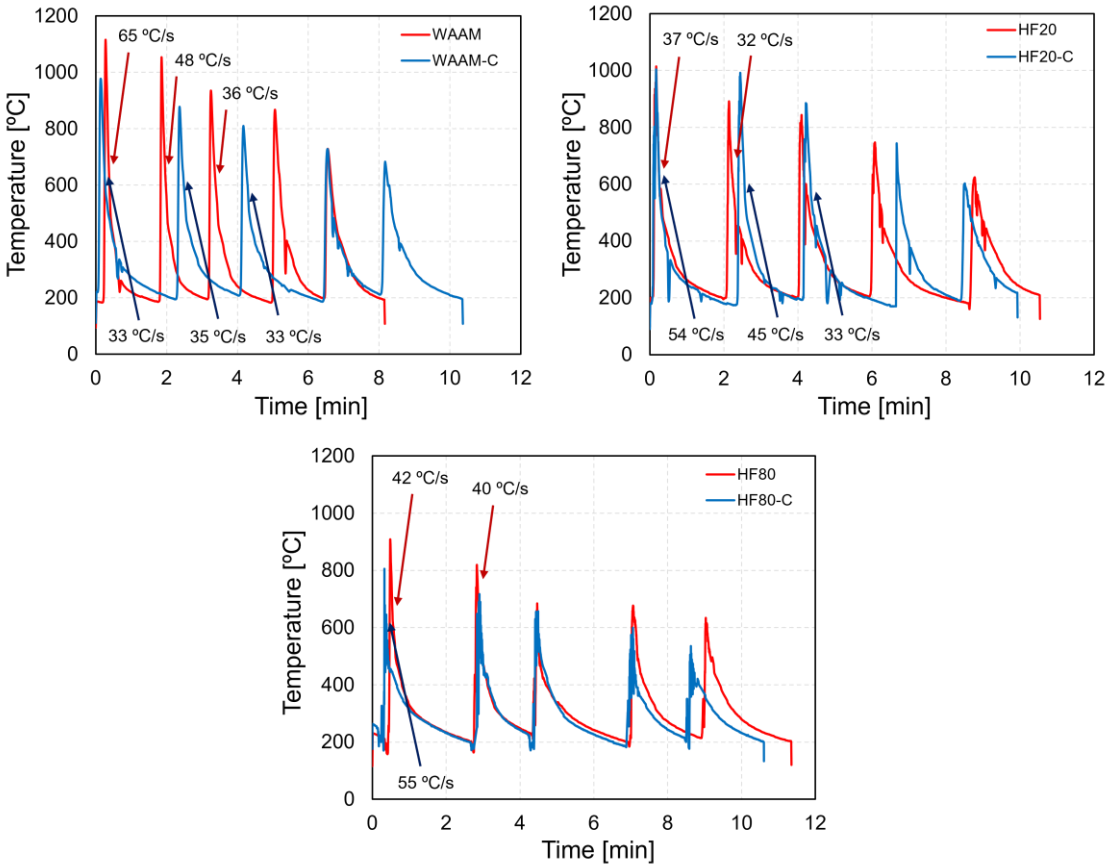

Figure 4.4 - Effect of the cooling system in the thermal cycles of the 7th layer for each sample

As expected, the use of the cooling system in the hammer combined with an 80% duty cycle (HF80-C) led to a reduction in peak temperature of 12%, where the peak temperature decreased from 915°C to 805°C. The WAAM-C sample experienced a similar reduction, with the peak temperature decreasing from 1115°C to 980°C. As a result, the reheating peak temperatures were also reduced. The sample produced with forging using a 20% duty cycle and cooling (HF20-C) was not able to lower the process temperature. This is due to the contact time between the hammer and the workpiece being insufficient to allow heat to be exchanged by conduction. Moreover, the trajectory of the hammer to perform the forging prevents an efficient heat transfer by convection, which can be confirmed by the inferior heat extraction efficiency compared to the WAAM-C process.

The WAAM sample showed the highest cooling rate (65 ºC/s) for the first thermal cycle of the 7th layer. Given that this sample had the highest peak temperature, there was a greater difference between the temperature of the environment and the temperature of the part, resulting in a higher cooling rate. In turn, samples manufactured with forging and cooling (HF20-C and HF80-C) experienced similar cooling rates, around 55 ºC/s. During the second thermal cycle, WAAM and HF20-C samples registered the highest cooling rates, 48 and 45 ºC/s, correspondingly. From the third cycle onwards, the samples showed similar cooling rates.

Furthermore, when comparing the samples fabricated without cooling, it is clear that the forging on its own also contributes to reducing the peak temperature of the workpiece. During the deposition of the 9th layer (3rd thermal cycle), the peak temperature reached in the 7th layer was about 950 ºC for the WAAM sample, 850 ºC for HF20 and 700 ºC for HF80. Since hot forging reduces the peak temperature of the reheating cycles, it can hinder transformations in the solid state, therefore altering the materials microstructure. This is particularly relevant in materials that undergo solid-state transformations, as is the case of the steel under study.

In order to evaluate the amount of heat exchanged by the coolant as it passed through the hammer's cooling channels, thermocouples were used at both the inlet and outlet of each channel to measure the temperature of the fluid. Figure 4.5 shows the evolution of the fluid temperature at both the inlet and outlet of one channel during the production of the WAAM-C sample, where each peak corresponds to the deposition of one layer.

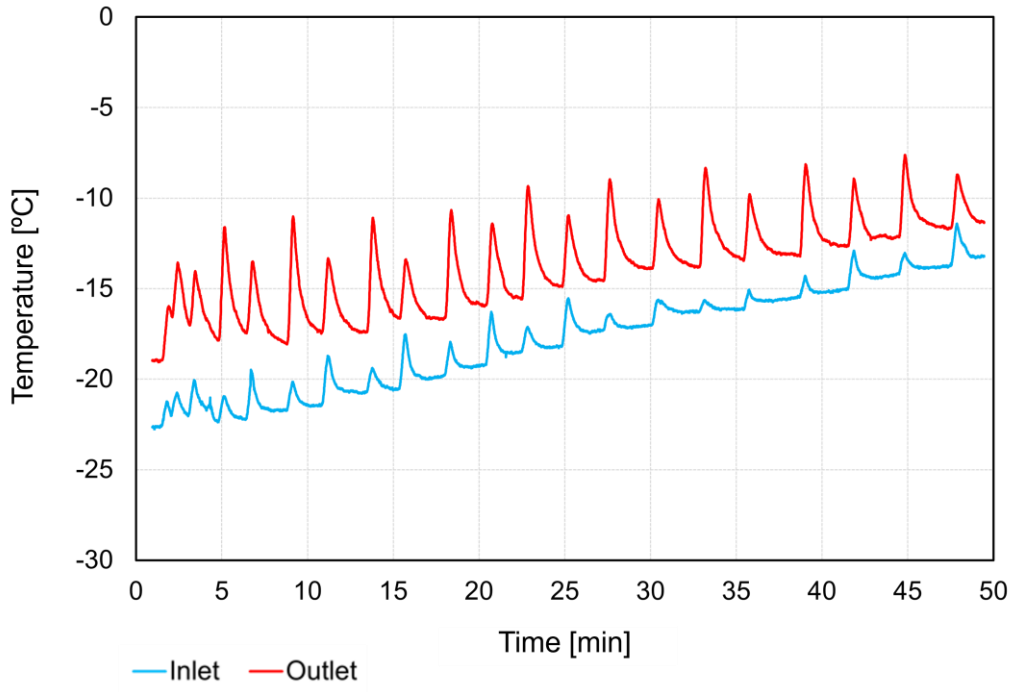

Figure 4.5 - Evolution of coolant temperature at both the inlet and outlet of one cooling channel during the production of the WAAM-C sample

It can be verified that the heat exchanged with the fluid was not constant, i.e., the cooling system lost efficiency throughout the process. At the beginning of the process, the heat exchanges reduced the fluid temperature by around 5.1 ºC, whereas in the last deposited layers, the temperature of the fluid decreased by around 3.1 ºC, in only one of the channels. The same trend was observed for the remaining samples. Nevertheless, this heat exchange occurred for the entire process, even without the deposition happening. Therefore, the temperature variation of the liquid in each cooling channel was analyzed, but only during deposition, to then calculate the thermal energy that was actually extracted from each sample. Thus, during the deposition of

the WAAM-C sample, the coolant temperature at the outlet increased 5.5 ºC at the beginning of the deposition and only 3.4 ºC at the end of the deposition, for the total of the 2 cooling channels.

The process parameters already presented were used to calculate a heat input of 295 J/mm and, given that the length of one layer was 120 mm, the total energy delivered to the workpiece during the deposition of one layer was 35400 J. Moreover, the amount of energy exchanged by the coolant during one deposition was calculated using Equation (4.*1*. Where m (kg) is the mass of fluid that passed through the cooling channels, C_p (J/kg ºC) is the specific heat of the liquid and ΔT (ºC) is the variation in temperature of the coolant during one deposition.

$$Q = mC_p\Delta T \tag{4.1}$$

Given that the coolant flow rate through one channel is 1.8 kg/min, the duration of one deposition is 0.30 min and the specific heat of the liquid is 3400 J/kg ºC, the amount of heat exchanged with the coolant, during the deposition of one layer, at the beginning, halfway through and at the end of the process was calculated. Table 4.2 shows these results, estimated for each sample, as well as the preponderance of energy consumed from the cooling system relative to the total energy provided to the part during the deposition of one layer.

Table 4.2 - Energy exchanged with the coolant during the deposition of one layer

Sample Reference	Deposition Stage	Energy Consumed (J)	Preponderance (%)
WAAM-C	Beginning	10098	29
	Middle	8834	25
	End	6242	18
HF20-C	Beginning	4406	12
	Middle	1877	5
	End	1728	4
HF80-C	Beginning	11200	32
	Middle	9954	28
	End	9027	25

These results confirm the loss of efficiency of the cooling system during the deposition of the 21 layers. The WAAM-C and HF80-C processes proved to be the most efficient at extracting thermal energy from the part, as was previously verified by the 12% reduction in the peak temperature. The sample produced by WAAM with cooling consumed 10098 J from the cooling

system in the deposition of one layer at the beginning of the process, 8834 J halfway through and only 6242 J at the end. Furthermore, the sample manufactured with forging under an 80% duty cycle and cooling (HF80-C) followed the same tendency, having exchanged 11200 J with the coolant when depositing one layer at the beginning of the process, 9954 J mid-way and 9027 J towards the end. Meanwhile, the sample fabricated with forging at a 20% duty cycle and cooling (HF20-C) was not efficient at removing heat from the workpiece, thus supporting the previous analyses on the thermal cycles experienced by the samples.

4.3 MICROSCOPIC CHARACTERIZATION

Figure 4.6 shows representative cross-section macrographs of the last seven deposited layers from the sample produced by the conventional WAAM process and from the samples produced with hot forging using an 80% duty cycle, with and without cooling, where it can be observed that forging has contributed to pore collapsing along the entire samples and grain refinement, particularly in the last layer.

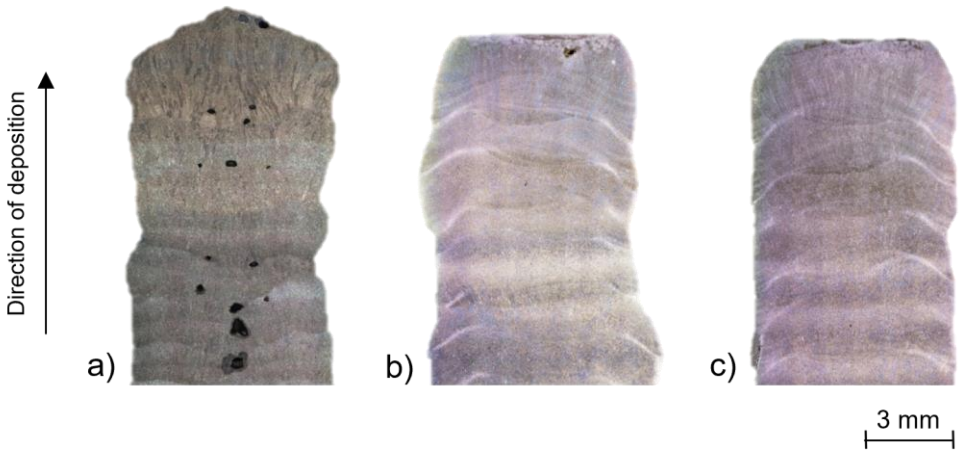

Figure 4.6 - Cross section macrograph of the last seven deposited layers for sample: a) WAAM; b) HF80; c) HF80-C

Despite the presence of some pores there were no cold cracks, which are common discontinuities in HSLA steels. In order to mitigate cold cracking in these steels, pre and post-heating techniques have been described in the welding literature. However, since in additive manufacturing the deposition is done layer by layer, the subsequent layers are responsible for increasing the temperature of the previous layers, resulting in a reduction of the material cooling rate in comparison to the single pass welding processes, which minimizes the possibility of cold crack formation [41]. Moreover, the absence of welding joints constraints allows the material to accumulate some of the thermal stresses generated during manufacturing, which also reduces the possibility of cold crack formation [41].

Figure 4.7 reveals the micrographs taken through optical microscopy of the last deposited layer from each produced part, where it can be seen that the resulting microstructures are in agreement with the cooling rates registered in the thermal analysis and are also aligned with the further microhardness results [37]. The microstructure analysis was performed on the last layer of each sample as this region was not subjected to the thermal reheating cycles that result from the deposition of subsequent layers, thus preserving the properties imposed by the hot forging, with and without cooling.

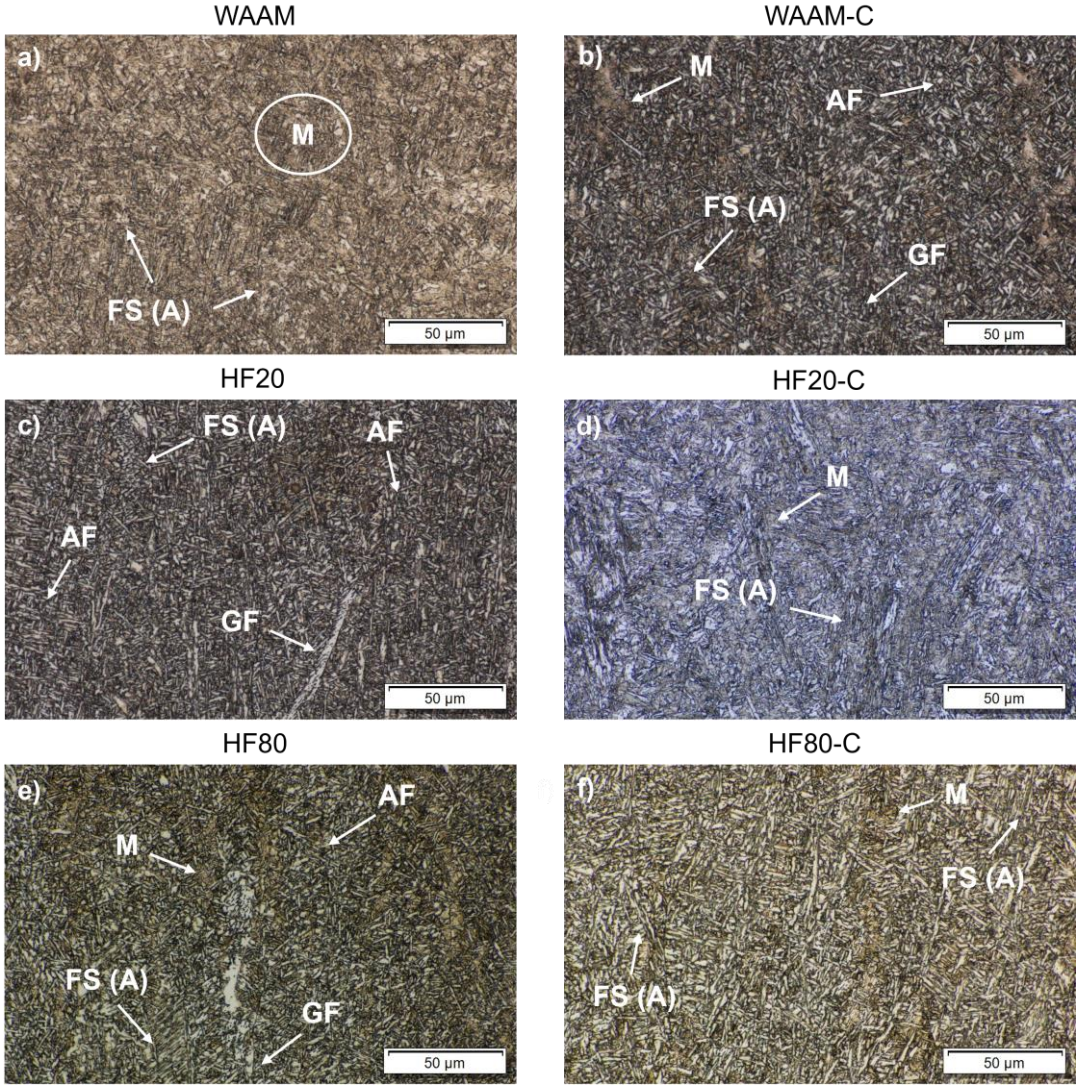

Figure 4.7 - Microstructure obtained in the last deposited layer of sample: a) WAAM; b) WAAM-C; c) HF20; d) HF20-C; e) HF80; f) HF80-C, where: AF - Acicular ferrite; FS - Ferrite with second phase aligned (A); GF - Grain boundary ferrite; M - Martensite

Due to the repeated reheating cycles, the microstructures of the samples were identical to the reheated weld metal of an HSLA steel weldment [41,42]. In this steel, the transformations in the solid state can be categorized into two temperature ranges with differing characteristics. During the first interval, from 1300 to 800 °C, there is a significant growth of austenite grains, whereas in the second interval, between 800 and 500 °C, the austenite is transformed into distinct ferrite and bainite morphologies [43].

Figure 4.8 shows the continuous cooling transformation (CCT) diagram of an HSLA steel, where the arrows indicate the cooling rates to be used as reference [37]. It can be verified that the previously identified microstructures are predicted by the diagram and are dependent on the material's cooling rate.

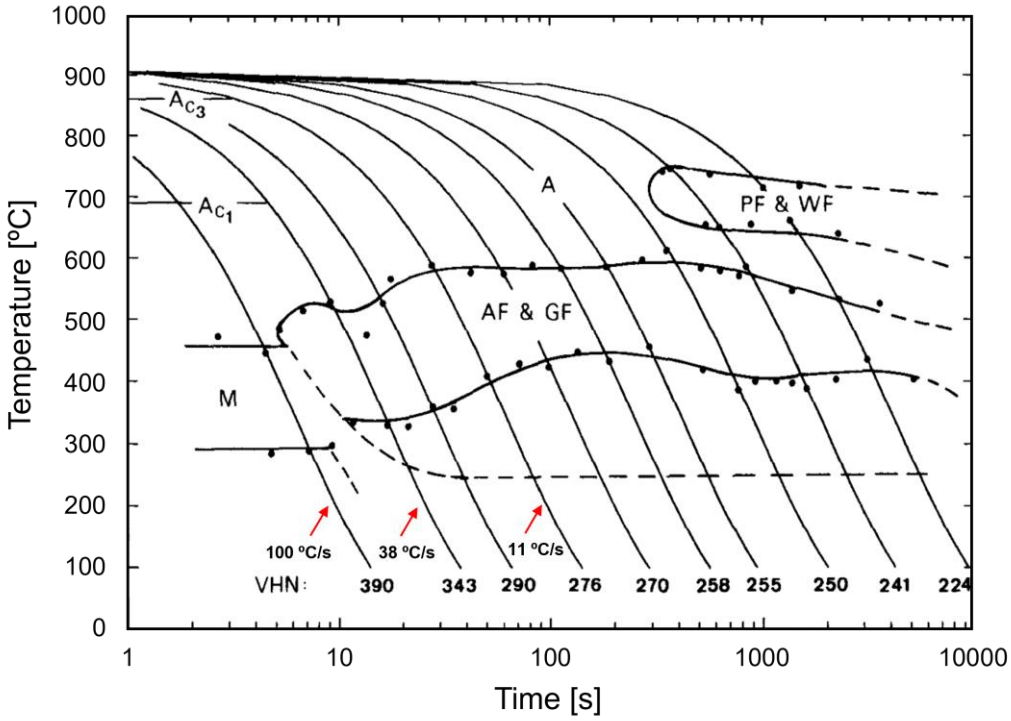

Figure 4.8 - CCT diagram for the HSLA steel (Adapted from [37])

Although martensite is promoted by an increase in the content of certain alloys, it can also be found in common C-Mn steels that have been welded with low heat input. Typically, this constituent exhibits high hardness and low ductility values and can cause local hydrogen embrittlement in the heat-affected zone (HAZ) [44]. The part manufactured through the conventional WAAM deposition process presented a lower quantity of constituents with lower hardness when compared to the other produced parts, which may lead to higher average microhardness values in the performed tests. This microstructure found in the WAAM sample suggests that it was caused by a greater cooling rate, due to the higher peak temperatures achieved during deposition. However, to achieve the formation of fully martensitic structures, it would be necessary to reach cooling rates of above 100 °C/s, which were not possible in this work. This kind of cooling rates can be attained, for example, during underwater welding [42].

Moreover, martensite can also be formed during the final cooling stage of the part to room temperature, where depending on the carbon content, any remaining austenite can be partially or totally transformed into martensite, which explains the formation of martensite in samples with lower cooling rates [41,44].

The acicular ferrite (AF) consists of tiny needles of ferrite that form in different orientations, creating the appearance of an interconnected microstructure. This needles form in intergranular regions and their transformation begins at temperatures close to 800 ºC [42]. Additionally, the formation of acicular ferrite is usually associated with cooling conditions, oxide inclusions and the hardenability of the weld metal [45].

After surpassing the high temperature cooling regime (1300 to 800 °C), austenite decomposes into ferrite, with the formation of grain boundary ferrite (GF) at the boundaries of the preceding austenite [41,42]. High quantities of this structure are not favorable for toughness, especially in high-strength steels. However, it was verified that this structure is not present in enough quantity to significantly influence the material's properties.

There are four different types of ferrite in the molten zone: grain boundary ferrite (GF), ferrite with second phase aligned (FS (A)), acicular ferrite (AF) and polygonal ferrite (PF) [46]. During cooling of the molten metal, grain boundary ferrite nucleates at the grain boundaries of the previous austenite at high temperatures, acting as a nucleation site for ferrite with second phase aligned, which protrudes from the grain boundaries into the previous austenite grains. As the heat input rises, the grain size increases, and the relative amount of AF and FS (A) decreases with the increase of GF and PF. Furthermore, the width of GF and FS (A) also increases with increasing welding heat input [46,47].

Figure 4.9 presents the micrographs obtained by optical microscopy from the middle of the cross section of the samples, where it can be seen that all samples obtained a similar structure, containing ferrite with second phase aligned (FS (A)) and martensite quenched (M_q). The sample produced by WAAM exhibited a greater amount of quenched martensite, which is why, despite the multiple thermal cycles, its hardness is slightly higher than the remaining samples. Moreover, the microstructure found in the middle of the samples was identical to the one found at the top, which suggests that the microstructure did not change along the height of the samples.

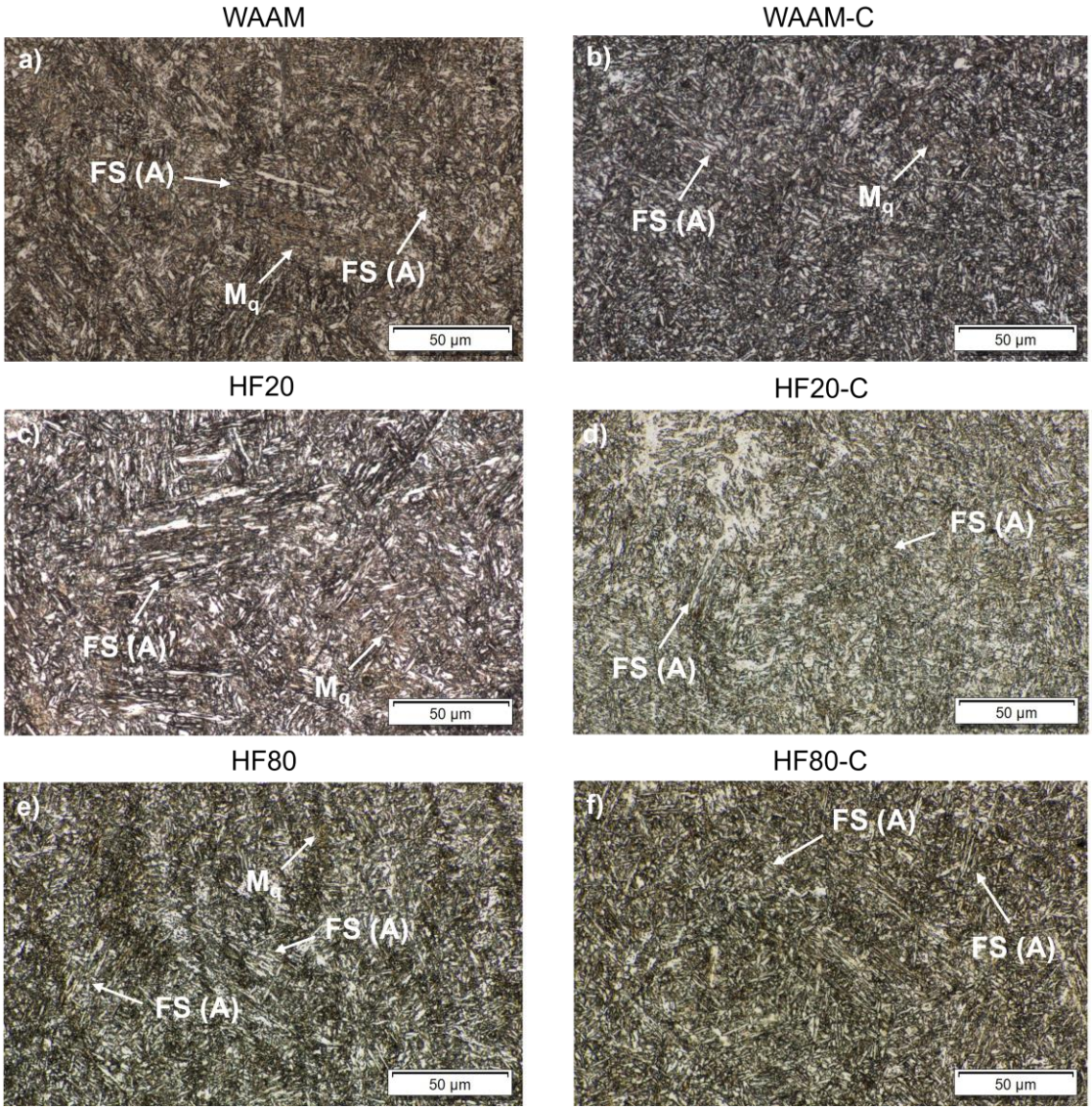

Figure 4.9 - Microstructure obtained in the middle of sample: a) WAAM; b) WAAM-C; c) HF20; d) HF20-C; e) HF80; f) HF80-C, where: FS - Ferrite with second phase aligned (A); M_q – Martensite quenched

Measuring or estimating previous austenitic grain sizes in materials under reheating cycles, as happens in WAAM, is challenging [48]. Therefore, a numerical simulation of the material was performed at a peak temperature of 900 °C, using different estimated grain sizes as the input parameters for the last deposited layer. Figure 4.10 shows the effect of grain size on the predicted microstructure for different grain sizes (10, 25, 50, 100, 500 and 1000 µm), where the red arrows indicate cooling rates of 100 °C/s and 10 °C/s to be used as reference.

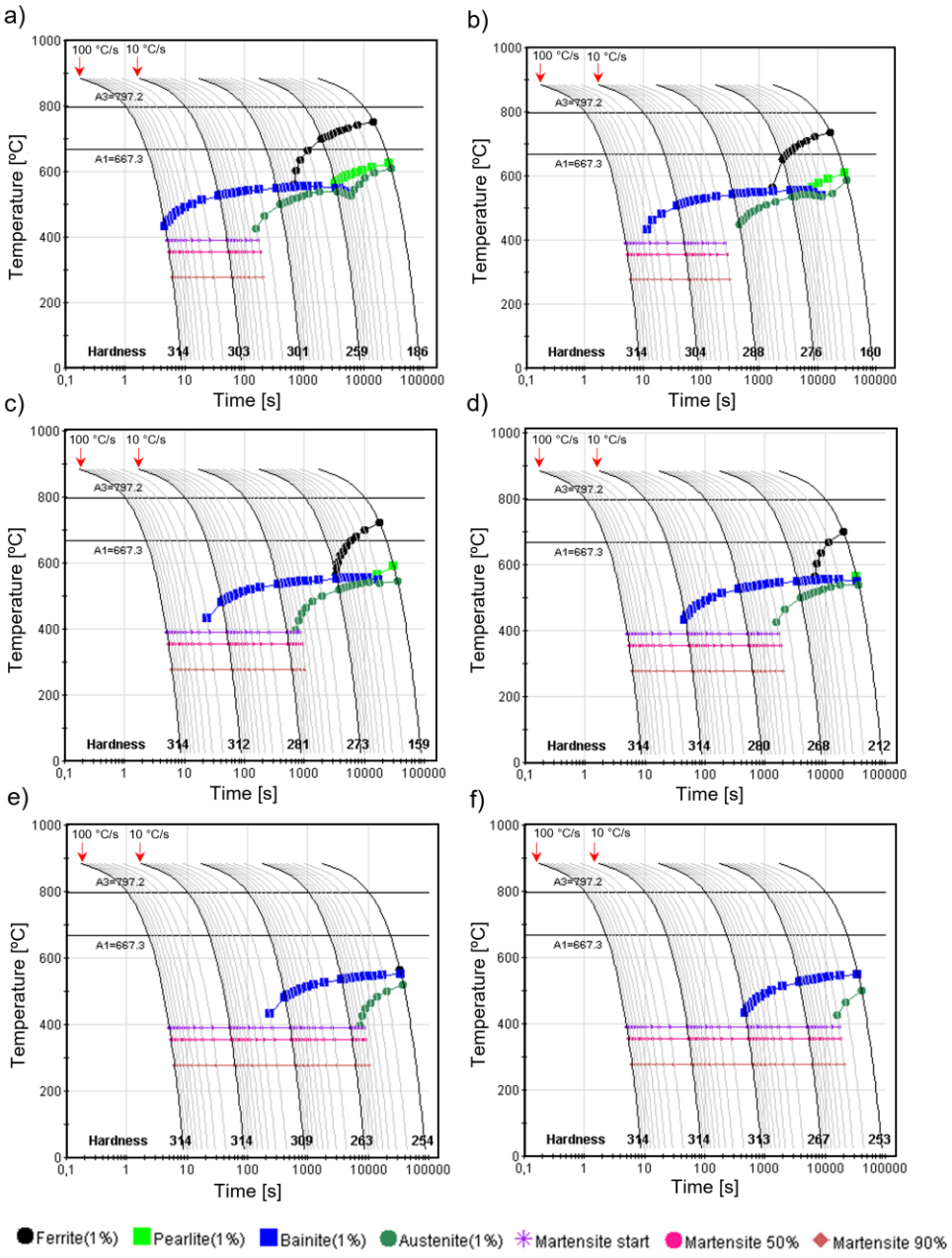

Figure 4.10 - Numerical simulation of the HSLA steel CCT diagram at a peak temperature of 900 ºC with increasing grain size of: a) 10 µm; b) 25 µm; c) 50 µm; d) 100 µm; e) 500 µm; f) 1000 µm

There is a notable difference in the microstructure results found in the diagram when changing grain size, where a reduction in hardenability is noticed with the reduction in grain size. Thus, for the same cooling rate, conditions with larger grains (e.g., 500 and 1000 µm) tend to present a greater volume of martensite (greater hardness). Furthermore, considering the cooling rates measured via thermography (Figure 4.4), it can be pointed out that the region unaffected by HF-WAAM, i.e., the region that remains with coarse columnar grains (~1000 µm) tends to have higher hardness values when compared to the deformed and recrystallized region, which has smaller austenite grains and is consequently less hardenable. For materials with a grain size of 1000 µm, bainite and austenite structures only form at low cooling rates, under 1 °C/s.

From these graphs it can be inferred that the use of the HF-WAAM process can cause the formation of less hard structures, since the hammer acts to refine the grains of the material after the deposition. This was already observed from Figure 4.7 and Figure 4.9, with a greater density of less hard structures in the samples manufactured by HF-WAAM compared to the sample manufactured by the conventional WAAM process. Moreover, the average hardness value found for the WAAM sample was higher, which can be attributed to the larger grain size, as observed in Figure 4.6, and to the higher cooling rate.

Nevertheless, it should be noted that the grain refinement effects generated by the hammer are more noticeable in the last layers and did not have a significant impact on the mechanical strength of the material, as shown in Figure 4.11. This is because, during deposition, each subsequent layer will fully or partially undergo austenitisation cycles at different peak temperatures. This tends to refine the grain of the previous austenite, which reduces its hardenability, generating a less hard structure, mainly composed of ferrite with a second aligned/non-aligned phase (bainite). Furthermore, if any martensite is still present, it will be quenched due to multiple heating cycles at subcritical temperatures. Thus, despite the grain refinement effect of austenite prior to the consequent drop in hardenability caused by HF-WAAM for the last layers, the typical allotropic transformation of low alloy steels and the multiple reheating cycles tend to extinguish the effect of HF-WAAM for the rest of the part, which is evidenced by the similar hardness values found between all conditions. Therefore, the present results indicate that the combination of the conventional WAAM deposition process with interlayer deformation may have a null or minimal effect for this alloy.

4.4 MICROHARDNESS TESTING

The results from the microhardness tests performed upon each of the six manufactured samples are depicted in Figure 4.11. WAAM and WAAM-C samples showed an average hardness value of 335 HV and 292 HV, correspondingly. Samples manufactured with forging and a 20% duty cycle presented an average hardness of 301 HV for that without cooling (HF20) and 300 HV for that with cooling (HF20-C). Samples produced with forging and an 80% duty cycle showed an average hardness value of 302 HV for that manufactured without cooling (HF80) and 281 HV for that with cooling (HF80-C).

These results indicate that there is no major difference in the microhardness profile between the various samples. However, there is a tendency for the hardness value to increase near the substrate, which could be associated to the dilution (increase in C content) and to the high cooling rates experienced in the first few layers, leading to the formation of martensite, as previously discussed. It is also possible to notice an increase in the hardness values in the last deposited layers, which may be related to the lack of multiple reheating cycles caused by the subsequent deposited layers, i.e., the tempering effect (softening) observed at the middle region of the samples was not verified in the last layers.

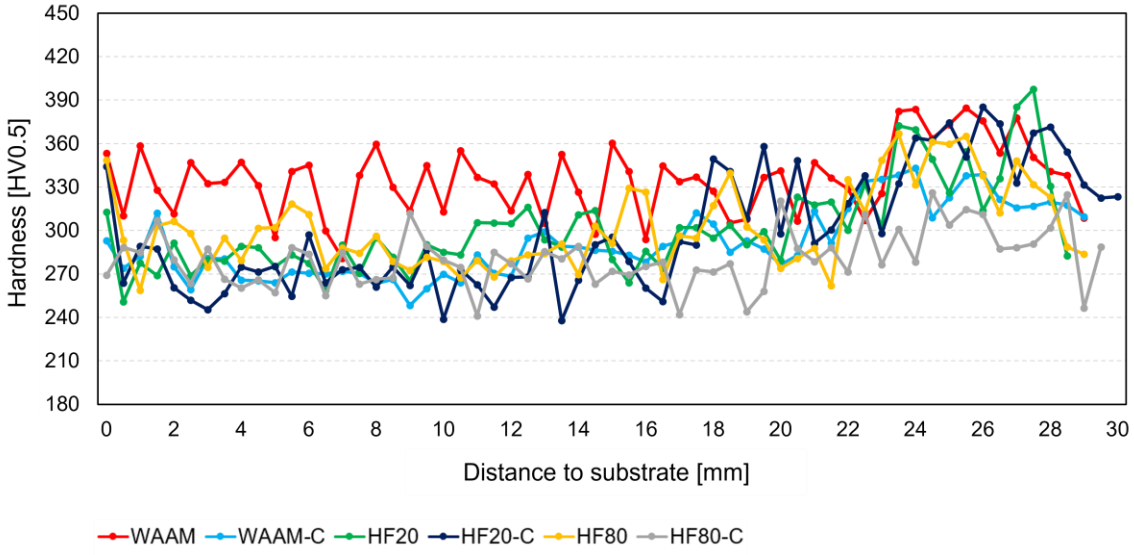

Figure 4.11 - Microhardness profiles for each produced sample

4.5 ELECTRICAL CONDUCTIVITY

The electrical conductivity of materials depends on the crystalline structure of the existing phases, the electronic mobility and the content of the existing defects, particularly punctual defects (voids), superficial defects (grain boundaries) and linear defects (dislocations). The electrical conductivity profile of the produced samples is presented in Figure 4.12. The same trend can be seen in all samples, with equal electrical conductivity in the substrate, followed by a decrease in the heat-affected zone, stabilizing again when the deposition begins. Thus, it is possible to categorize the samples into three metallographic structures with different characteristics.

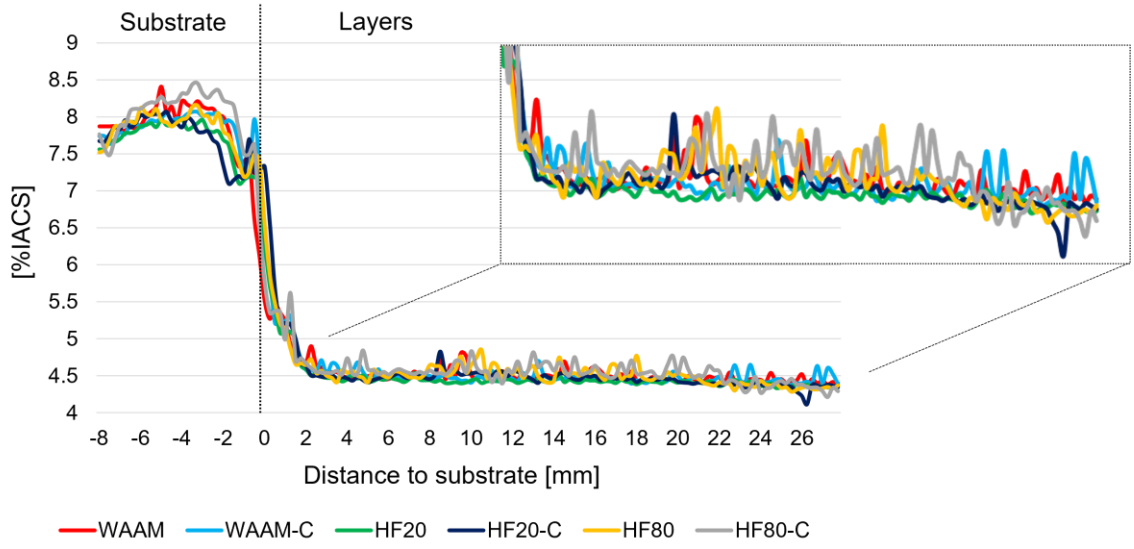

Figure 4.12 - Electrical conductivity of each manufactured part

The substrate is the region characterized by having large grains with minimum microstructural changes, which facilitates the passage of electric current. The HAZ is characterized by an increase in grain size and dilution caused by the mixture between the deposited material and the substrate. The increase in grain size leads to a decrease in grain boundaries, making it easier for the electric current to pass through. In turn, dilution causes a drop in electrical conductivity due to the alloying elements that become obstacles to the passage of electrical current. As soon as deposition begins, the electrical conductivity levels off, maintaining a lower value than that in the substrate. It is also notable that samples produced with 20% duty cycle present greater uniformity in electrical conductivity throughout the height, suggesting a more homogeneous microstructure than in the remaining samples.

The results indicate that there are no microstructural differences or any major variation in the grain size of the manufactured parts, as demonstrated by the micrographic analysis. Moreover, it can be verified that there is a positive correlation between the general characteristics of the microstructure of the parts and the four-point electrical conductivity test, as has been described by other authors [49–51].

4.6 UNIAXIAL TENSILE TESTING

Additive manufactured parts typically feature anisotropic properties, i.e., they show different behavior and properties in vertical and horizontal directions, mainly influenced by temperature gradients that vary between the deposition of consecutive layers [52]. In general, vertical (transverse) specimens have lower mechanical strength than the horizontal (longitudinal) ones since they are manufactured vertically to the direction of the deposition and have more interlayers in the testing region [52–54]. The interlayer region is, in some materials, considered to be the most critical as it accumulates residual stress and undergoes greater microstructural changes caused by successive thermal cycles [55].

Uniaxial tensile tests were carried out in both longitudinal (Y) and transverse (Z) directions on samples without macroscopic defects. Ultimate Tensile Strength (UTS), yield strength and elongation to fracture were calculated and the results are presented in Figure 4.13. Data on the ER110S-G wire given by the manufacturer is also included for comparison.

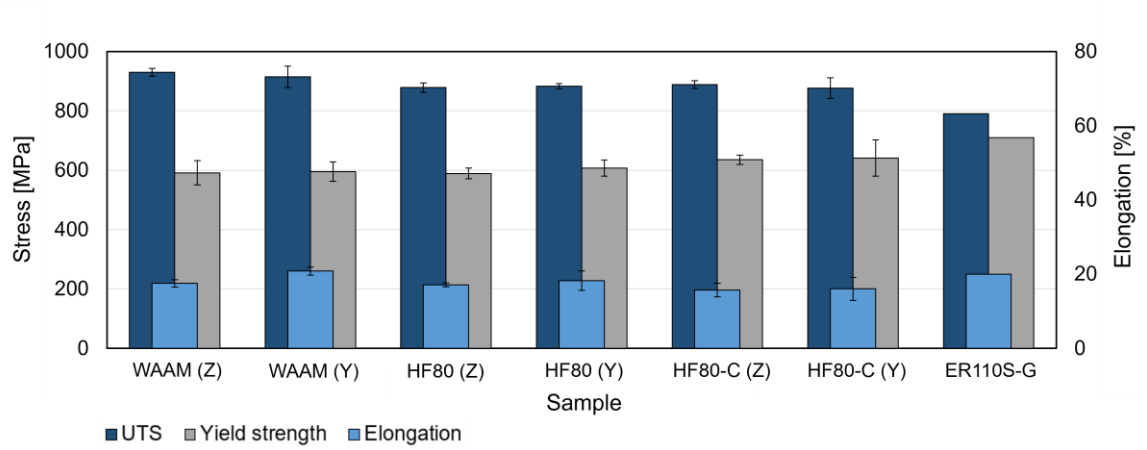

Figure 4.13 - Results from the uniaxial tensile tests performed in samples WAAM, HF80 and HF80-C

There were no significant variations in the mechanical properties of the specimens extracted in the transverse and longitudinal directions. The UTS registered an anisotropy of 1.6% for the sample obtained by WAAM, 0.6% for the sample manufactured with hot forging using an 80% duty cycle (HF80) and 1.4% for the sample produced with hot forging and cooling (HF80-C). These small variations indicate that the samples produced do not present significant changes in their mechanical properties in the various regions analyzed. Some literature works have revealed anisotropy values of between 2 and 40% for different materials and additive manufacturing techniques [52–57]. For parts manufactured from low carbon steel using the conventional WAAM process, anisotropy values of between 4 and 20% were found in the literature for the UTS and up to 61% for the elongation values, which demonstrates the positive results achieved in this work [52,55,58,59].

Furthermore, every sample registered an increase in their UTS values in comparison with the value provided by the manufacturer for the ER110S-G wire, which is 790 MPa. The WAAM sample recorded slightly higher UTS values, between 4 and 6% higher according to specimen orientation, when compared to the HF80 and HF80-C samples. Nevertheless, the samples HF80 and HF80-C registered lower anisotropy values.

When analyzing the mechanical strength of specimens manufactured with forging, it appears that cooling the hammer had no major impact on the UTS and yield strength results, with an increase of just 1% in the average UTS value and a 7% increase in the average yield strength value for the transverse specimens extracted from the sample produced with hot forging and cooling (HF80-C). Regarding the longitudinal specimens, the HF80-C sample showed an increase of 5% in the average yield strength and a reduction of 1% in the average UTS. Moreover, the sample manufactured with forging and cooling exhibited a 1% reduction in the average elongation to fracture value for transverse specimens and a 2% reduction for the longitudinal ones. Representative stress-strain curves for specimens extracted in both transverse and longitudinal orientation from the HF80-C sample are shown in Figure 4.14.

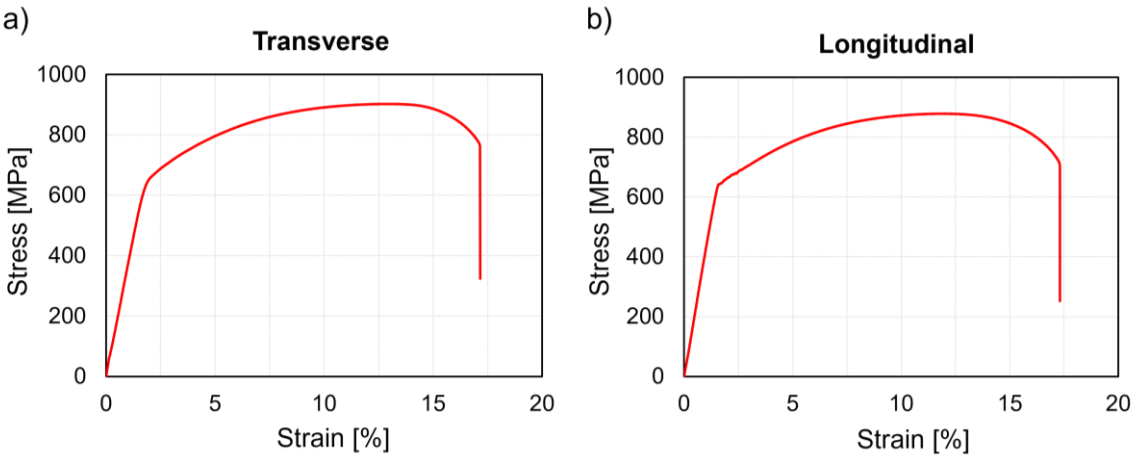

Figure 4.14 - Uniaxial tensile stress-strain curve for the HF80-C sample of specimen extracted in the: a) transverse direction; b) longitudinal direction

4.7 FRACTOGRAPHY

The fracture surfaces of specimens submitted to the uniaxial tensile tests were inspected with a Scanning Electron Microscope (SEM) and are presented in Figure 4.15. It can be observed that the fracture surfaces are rough with a clear ductile aspect, which is characterized by growth and coalescence of microscopic voids (dimples). Generally, ductile materials fail due to the nucleation, growth and coalescence of microvoids that initiate in inclusions and second-phase particles [60]. The dimples have an irregular shape because the microvoids appear randomly, however, the shape that they appear in the microscope depends on the stress system that was acting during their formation and the angle of observation in the microscope [61]. In this case, the formation of equiaxial dimples was observed since the actuating stresses were mainly tensile. The WAAM-C sample had pores with a size that covered nearly the entire cross-section of the microspecimen. Nonetheless, the tested and fractured region also exhibited ductile fracture characteristics, as did the other samples.

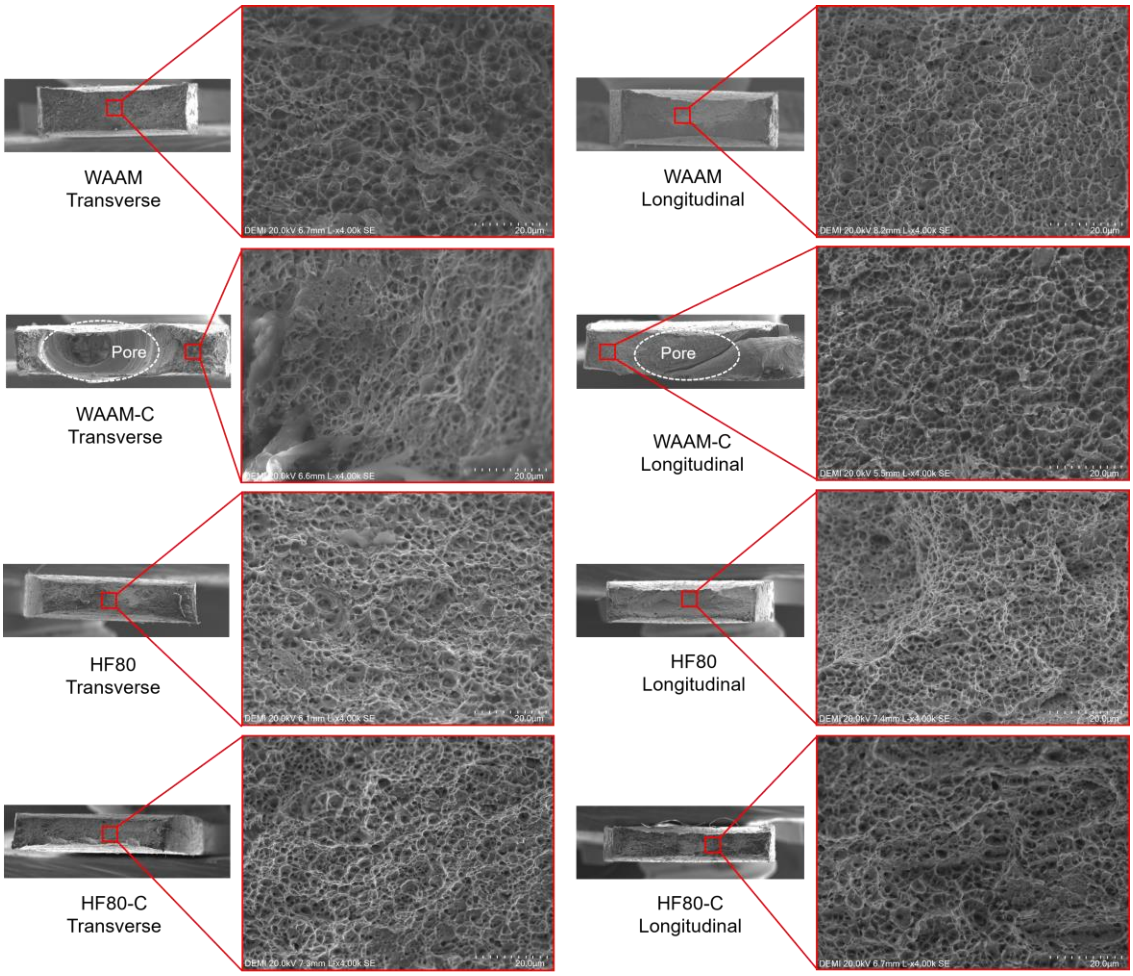

Figure 4.15 - Fracture surface from the uniaxial tensile test of transverse and longitudinal specimens taken from samples: WAAM, WAAM-C, HF20, HF20-C, HF80 and HF80-C

Figure 4.16 illustrates the fracture surfaces of specimens taken from the samples manufactured by WAAM, with and without cooling, and from the samples manufactured with hot forging at an 80% duty cycle, with and without cooling, and it shows the small spherical inclusion that generated nucleation and dimple formation. During the uniaxial tensile test, large shear deformations can occur in the material but a small amount of material around the particle will not participate in the deformation, which will cause a defect between the particle and its immediate surroundings. Tension increases in this region and when it reaches high values, microvoids appear as a result of the particle breaking or the interface decohesion [60,61].

The sizes of the dimples are shaped according to the existing spaces between adjacent microvoids and according to the type and dimensions of the inclusions [62]. It is clear that for each sample shown in Figure 4.16, the size and quantity of dimples is regular, which indicates that the samples did not have different types of randomly distributed inclusions. Nevertheless, it can be seen that the samples produced by WAAM had larger dimples compared to the samples produced with forging.

It can be verified that samples manufactured by WAAM had larger dimples than those manufactured by HF-WAAM. The WAAM and WAAM-C samples showed an average dimple size of 1.42 µm and 1.51 µm, respectively, whereas HF80 and HF80-C samples had an average dimple size of 1.20 µm and 1.07 µm, correspondingly. Materials with lower ductility and a higher number of impurities exhibit a higher number of dimples, with smaller dimensions [61]. This behaviour was also confirmed by the tensile test, in which the samples manufactured by WAAM showed, on average, higher elongation to fracture values. Thus, it is possible to state that forging influenced the quantity of dimples generated, either by promoting a greater number of nucleation sites during solidification or by inducing residual dislocations that enables the grain recrystallisation during the next deposited layer. The same phenomenon has been verified by other authors when using cold roll forging during the WAAM process [63].

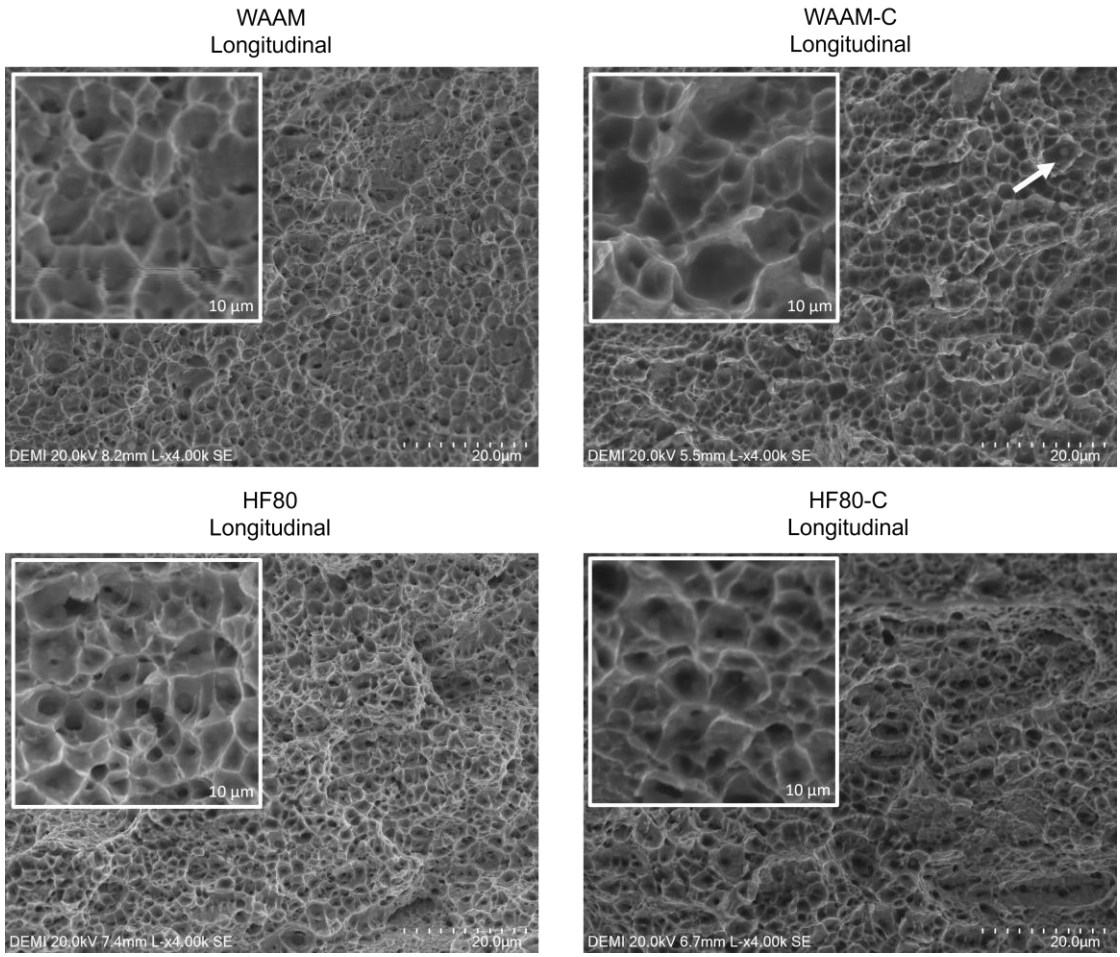

Figure 4.16 - Fracture surface from the uniaxial tensile test of longitudinal specimens taken from samples: WAAM, WAAM-C, HF80 and HF80-C

5 CONCLUSIONS AND FUTURE WORK

5.1 CONCLUSIONS

This work had as its primary purpose the design and study of a new variant for the WAAM process based on the combination of mechanical deformation and temperature control to overcome its main shortcomings and thus contribute to its industrialization. Based on the results obtained, it is possible to conclude the following:

- All samples contained constituents that were predicted by the CCT diagram of the HSLA steel for the corresponding cooling rates.
- The use of the cooling system combined with hot forging at an 80% duty cycle lowered the average temperature of the hammer by 90 °C, which represents a 77% reduction. Moreover, it led to a reduction in peak temperature of 12%, where the peak temperature decreased from 915°C to 805°C.
- The cooling rate was higher in the conventional WAAM process due to the higher peak temperature reached during the thermal cycles. As a result, this sample presented fewer of the less hard constituents, as observed through optical microscopy and confirmed by the hardness test.
- The manufactured parts registered an increase in tensile strength, with an anisotropy of under 2%.
- No differences were found in the mechanical strength of the parts produced by WAAM and HF-WAAM, with and without cooling, meaning that the use of the hammer and the cooling system did not influence this aspect.
- The WAAM-C sample showed an excessive quantity of pores which impeded the tensile test to be performed. Furthermore, it was found that the use of the hammer led to a considerable reduction in quantity and size of pores.
- Every sample exhibited ductile fracture characteristics after the uniaxial tensile test, as evidenced by fractography.
- Hot forging contributed to a refined microstructure by reducing grain size and causing a slight reduction in ductility.

- The eddy current testing revealed a decrease of the electrical conductivity in the deposited layers in comparison to the substrate region. The test was sensitive in predicting different microstructures between the substrate, HAZ and deposited layers.

5.2 FUTURE WORK

From the experience gathered in this work, some improvements and proposals for future work are suggested which are summarized in this section.

Improvements to the cooling system are recommended, with the use of a fully isolated refrigeration chamber and separate tanks for the coolant inlet and outlet. Moreover, it is suggested that the parts be deposited with a lower inlet temperature for the coolant to maximize the temperature differential. To further increase the cooling rate and refine the microstructure, a cooled device should be used to keep on removing heat from the workpiece by conduction after the torch and hammer have passed through.

To determine the static mechanical strength of the manufactured parts, uniaxial tensile tests were performed on specimens with different orientations. In order to characterize the materials' behavior under dynamic loading, it is suggested that fatigue tests be carried out on the samples produced by WAAM and HF-WAAM, with and without cooling.

Given that in many applications the materials are exposed to collisions, it is recommended that the materials be also characterized through impact testing. As these are temperature sensitive, it is suggested that a wide temperature range be used for a more extensive characterization that covers a greater variety of applications.

6 REFERENCES

[1] T. DebRoy, H.L. Wei, J.S. Zuback, T. Mukherjee, J.W. Elmer, J.O. Milewski, A.M. Beese, A. Wilson-Heid, A. De, W. Zhang, Additive manufacturing of metallic components – Process, structure and properties, Prog. Mater. Sci. 92 (2018) 112–224. https://doi.org/10.1016/j.pmatsci.2017.10.001.

[2] V. Duarte, Developments in Directed Energy Deposition Additive Manufacturing: In-situ Hot Forging and Indirect Cooling, NOVA University Lisbon, 2022.

[3] ISO/ASTM-52900:2015, Additive manufacturing - General principles - Terminology, (2015).

[4] Ivántabernero, A. Paskual, P. Álvarez, A. Suárez, Study on Arc Welding Processes for High Deposition Rate Additive Manufacturing, Procedia CIRP. 68 (2018) 358–362. https://doi.org/10.1016/J.PROCIR.2017.12.095.

[5] T.A. Rodrigues, V. Duarte, R.M. Miranda, T.G. Santos, J.P. Oliveira, Current Status and Perspectives on Wire and Arc Additive Manufacturing (WAAM), Materials (Basel). 12 (2019) 1121. https://doi.org/10.3390/ma12071121.

[6] J.P.M. Pragana, R.F.V. Sampaio, I.M.F. Bragança, C.M.A. Silva, P.A.F. Martins, Hybrid metal additive manufacturing: A state–of–the-art review, Adv. Ind. Manuf. Eng. 2 (2021) 100032. https://doi.org/10.1016/j.aime.2021.100032.

[7] O.J. Santos, L. Quintino, Processos de soldadura, Lisboa, 1998.

[8] ASM International, Welding, Brazing, and Soldering, 1993.

[9] Gene Mathers, The welding of aluminium and its alloys, 1st ed., Woodhead Publishing, 2002.

[10] W. Ou, T. Mukherjee, G.L. Knapp, Y. Wei, T. DebRoy, Fusion zone geometries, cooling rates and solidification parameters during wire arc additive manufacturing, Int. J. Heat Mass Transf. 127 (2018) 1084–1094. https://doi.org/10.1016/j.ijheatmasstransfer.2018.08.111.

[11] T. Rodrigues, Wire and arc additive manufacturing: equipment development and parts characterization, NOVA School of Science and Technology, 2018.

[12] H.E. Coules, P. Colegrove, L.D. Cozzolino, S.W. Wen, Experimental measurement of biaxial thermal stress fields caused by arc welding, J. Mater. Process. Technol. 212 (2012) 962–968. https://doi.org/10.1016/j.jmatprotec.2011.12.006.

[13] B. Tomar, S. Shiva, T. Nath, A review on wire arc additive manufacturing: Processing parameters, defects, quality improvement and recent advances, Mater. Today Commun. 31 (2022) 103739. https://doi.org/10.1016/j.mtcomm.2022.103739.

[14] M.P. Mughal, R.A. Mufti, H. Fawad, The mechanical effects of deposition patterns in welding-based layered manufacturing, Proc. Inst. Mech. Eng. Part B J. Eng. Manuf. 221 (2007) 1499–1509. https://doi.org/10.1243/09544054JEM783.

[15] V.I. Ryazantsev, V.A. Fedoseev, Metallurgical and technological porosity of aluminium alloys in arc welding, Weld. Int. 16 (2002) 320–324. https://doi.org/10.1080/09507110209549538.

[16] E.M. Ryan, T.J. Sabin, J.F. Watts, M.J. Whiting, The influence of build parameters and wire batch on porosity of wire and arc additive manufactured aluminium alloy 2319, J. Mater. Process. Technol. 262 (2018) 577–584. https://doi.org/10.1016/j.jmatprotec.2018.07.030.

[17] A. Lopez, R. Bacelar, I. Pires, T.G. Santos, J.P. Sousa, L. Quintino, Non-destructive testing application of radiography and ultrasound for wire and arc additive manufacturing, Addit. Manuf. 21 (2018) 298–306. https://doi.org/10.1016/j.addma.2018.03.020.

[18] P.A. Colegrove, H.E. Coules, J. Fairman, F. Martina, T. Kashoob, H. Mamash, L.D. Cozzolino, Microstructure and residual stress improvement in wire and arc additively manufactured parts through high-pressure rolling, J. Mater. Process. Technol. 213 (2013) 1782–1791. https://doi.org/10.1016/j.jmatprotec.2013.04.012.

[19] F. Martina, P.A. Colegrove, S.W. Williams, J. Meyer, Microstructure of Interpass Rolled Wire + Arc Additive Manufacturing Ti-6Al-4V Components, Metall. Mater. Trans. A. 46 (2015) 6103–6118. https://doi.org/10.1007/s11661-015-3172-1.

[20] J.R. Hönnige, P.A. Colegrove, S. Ganguly, E. Eimer, S. Kabra, S. Williams, Control of residual stress and distortion in aluminium wire + arc additive manufacture with rolling, Addit. Manuf. 22 (2018) 775–783. https://doi.org/10.1016/j.addma.2018.06.015.

[21] J.R. Hönnige, P.A. Colegrove, B. Ahmad, M.E. Fitzpatrick, S. Ganguly, T.L. Lee, S.W. Williams, Residual stress and texture control in Ti-6Al-4V wire + arc additively manufactured intersections by stress relief and rolling, Mater. Des. 150 (2018) 193–205. https://doi.org/10.1016/j.matdes.2018.03.065.

[22] J.R. Hönnige, P. Colegrove, S. Williams, Improvement of microstructure and mechanical properties in Wire + Arc Additively Manufactured Ti-6Al-4V with Machine Hammer Peening, Procedia Eng. 216 (2017) 8–17. https://doi.org/10.1016/j.proeng.2018.02.083.

[23] L. Neto, S. Williams, J. Ding, J. Hönnige, F. Martina, Mechanical Properties Enhancement of Additive Manufactured Ti-6Al-4V by Machine Hammer Peening, in: 2020: pp. 121–132. https://doi.org/10.1007/978-981-15-0054-1_13.

[24] Z. Hai-ou, R. Wang, L. Liang, W. Gui-lan, HDMR technology for the aircraft metal part, Rapid Prototyp. J. 22 (2016) 857–863. https://doi.org/10.1108/RPJ-05-2015-0047.

[25] V.R. Duarte, T.A. Rodrigues, N. Schell, R.M. Miranda, J.P. Oliveira, T.G. Santos, Hot forging wire and arc additive manufacturing (HF-WAAM), Addit. Manuf. 35 (2020) 101193. https://doi.org/10.1016/j.addma.2020.101193.

[26] V.R. Duarte, T.A. Rodrigues, N. Schell, R.M. Miranda, J.P. Oliveira, T.G. Santos, In-situ hot forging directed energy deposition-arc of CuAl8 alloy, Addit. Manuf. 55 (2022) 102847. https://doi.org/10.1016/j.addma.2022.102847.

[27] H. Geng, J. Li, J. Xiong, X. Lin, Optimisation of interpass temperature and heat input for wire and arc additive manufacturing 5A06 aluminium alloy, Sci. Technol. Weld. Join. 22 (2017) 472–483. https://doi.org/10.1080/13621718.2016.1259031.

[28] F. Montevecchi, G. Venturini, N. Grossi, A. Scippa, G. Campatelli, Idle time selection for wire-arc additive manufacturing: A finite element-based technique, Addit. Manuf. 21 (2018) 479–486. https://doi.org/10.1016/j.addma.2018.01.007.

[29] V.T. Le, D.S. Mai, H. Paris, Influences of the compressed dry air-based active cooling on external and internal qualities of wire-arc additive manufactured thin-walled SS308L components, J. Manuf. Process. 62 (2021) 18–27. https://doi.org/10.1016/j.jmapro.2020.11.046.

[30] B. Wu, Z. Pan, D. Ding, D. Cuiuri, H. Li, Z. Fei, The effects of forced interpass cooling on the material properties of wire arc additively manufactured Ti6Al4V alloy, J. Mater. Process. Technol. 258 (2018) 97–105. https://doi.org/10.1016/j.jmatprotec.2018.03.024.

[31] L.J. da Silva, D.M. Souza, D.B. de Araújo, R.P. Reis, A. Scotti, Concept and validation of an active cooling technique to mitigate heat accumulation in WAAM, Int. J. Adv. Manuf. Technol. 107 (2020) 2513–2523. https://doi.org/10.1007/s00170-020-05201-4.

[32] X. Bai, H. Zhang, G. Wang, Modeling of the moving induction heating used as secondary heat source in weld-based additive manufacturing, Int. J. Adv. Manuf. Technol. 77 (2015) 717–727. https://doi.org/10.1007/s00170-014-6475-2.

[33] T.A. Rodrigues, V.R. Duarte, D. Tomás, J.A. Avila, J.D. Escobar, E. Rossinyol, N. Schell, T.G. Santos, J.P. Oliveira, In-situ strengthening of a high strength low alloy steel during Wire and Arc Additive Manufacturing (WAAM), Addit. Manuf. 34 (2020) 101200. https://doi.org/10.1016/j.addma.2020.101200.

[34] J.R. Kennedy, A.E. Davis, A.E. Caballero, S. Williams, E.J. Pickering, P.B. Prangnell, The potential for grain refinement of Wire-Arc Additive Manufactured (WAAM) Ti-6Al-4V by ZrN and TiN inoculation, Addit. Manuf. 40 (2021) 101928. https://doi.org/10.1016/j.addma.2021.101928.

[35] W. Hackenhaar, F. Montevecchi, A. Scippa, G. Campatelli, Air-Cooling Influence on Wire Arc Additive Manufactured Surfaces, Key Eng. Mater. 813 (2019) 241–247.

[36] B. Massalski, T, Binary Alloy Phase Diagrams, 2nd Editio, ASM International, 2018. https://doi.org/10.31399/asm.hb.v03.a0006247.

[37] S.W. Thompson, D.J. Vin Col, G. Krauss, Continuous cooling transformations and microstructures in a low-carbon, high-strength low-alloy plate steel, Metall. Trans. A. 21 (1990) 1493–1507. https://doi.org/10.1007/BF02672564.

[38] Lincoln Electric 1.2 mm Solid Wire EN ISO 16834-A AWS, (2016). https://www.lincolnelectric.com/assets/global/Products/ConsumableEU_MIGWires-LNM-LNMMoNiVa/lnmmoniva-eng.pdf (accessed February 15, 2023).

[39] D. Yang, G. Wang, G. Zhang, Thermal analysis for single-pass multi-layer GMAW based additive manufacturing using infrared thermography, J. Mater. Process. Technol. 244 (2017) 215–224. https://doi.org/10.1016/J.JMATPROTEC.2017.01.024.

[40] N. Kashaev, M. Horstmann, V. Ventzke, S. Riekehr, N. Huber, Comparative study of mechanical properties using standard and micro-specimens of base materials Inconel 625, Inconel 718 and Ti-6Al-4 V, J. Mater. Res. Technol. 2 (2013) 43–47. https://doi.org/10.1016/J.JMRT.2013.03.003.

[41] T.A. Rodrigues, V. Duarte, J.A. Avila, T.G. Santos, R.M. Miranda, J.P. Oliveira, Wire and arc additive manufacturing of HSLA steel: Effect of thermal cycles on microstructure and mechanical properties, Addit. Manuf. 27 (2019) 440–450. https://doi.org/10.1016/J.ADDMA.2019.03.029.

[42] G.F. Vander Voort, Metallography of Welds in Carbon-manganese Steels: Introductory Notes, McGraw-Hill Inc., 1984.

[43] Y. Shi, Z. Han, Effect of weld thermal cycle on microstructure and fracture toughness of simulated heat-affected zone for a 800 MPa grade high strength low alloy steel, J. Mater. Process. Technol. 207 (2008) 30–39. https://doi.org/10.1016/J.JMATPROTEC.2007.12.049.

[44] C. Capdevila, F.G. Caballero, C.G. de Andrés, Determination of Ms Temperature in Steels: A Bayesian Neural Network Model., ISIJ Int. 42 (2002) 894–902. https://doi.org/10.2355/isijinternational.42.894.

[45] S.S. Babu, The mechanism of acicular ferrite in weld deposits, Curr. Opin. Solid State Mater. Sci. 8 (2004) 267–278. https://doi.org/10.1016/J.COSSMS.2004.10.001.

[46] W. Gao, D. Wang, F. Cheng, X. Di, C. Deng, W. Xu, Microstructural and mechanical performance of underwater wet welded S355 steel, J. Mater. Process. Technol. 238 (2016) 333–340. https://doi.org/10.1016/J.JMATPROTEC.2016.07.039.

[47] L.E. Ramírez Luna, A.Q. Bracarense, E.C.P. Pessoa, P.S. Costa, G. Altamirano Guerrero, A.E. Salas Reyes, Effect of the welding angle on the porosity of underwater wet welds performed in overhead position at different simulated depths, J. Mater. Process. Technol. 294 (2021) 117114. https://doi.org/10.1016/J.JMATPROTEC.2021.117114.

[48] M. Högström, A. Fadaei, A. Rahimi, P. Li, M. Igestrand, J. Andersson, A. Scotti, Proposal and Assessment of a Multiple Cycle-Continuous Cooling Transformation (MC-CCT) Diagram for Wire Arc Additive Manufacturing of Thin Walls, Metals (Basel). 13 (2023) 1533. https://doi.org/10.3390/met13091533.

[49] P.M. Ferreira, M.A. Machado, M.S. Carvalho, C. Vidal, Granting Sensorial Properties to Metal Parts through Friction Stir Processing, Measurement. 207 (2023) 112405. https://doi.org/10.1016/J.MEASUREMENT.2022.112405.

[50] G.L. Sorger, J.P. Oliveira, P.L. Inácio, N. Enzinger, P. Vilaça, R.M. Miranda, T.G. Santos, Non-destructive microstructural analysis by electrical conductivity: Comparison with hardness measurements in different materials, J. Mater. Sci. Technol. 35 (2019) 360–368. https://doi.org/10.1016/J.JMST.2018.09.047.

[51] T.A. Rodrigues, F.W. Cipriano Farias, K. Zhang, A. Shamsolhodaei, J. Shen, N. Zhou, N. Schell, J. Capek, E. Polatidis, T.G. Santos, J.P. Oliveira, Wire and arc additive manufacturing of 316L stainless steel/Inconel 625 functionally graded material: development and characterization, J. Mater. Res. Technol. 21 (2022) 237–251. https://doi.org/10.1016/J.JMRT.2022.08.169.

[52] L. Sun, F. Jiang, R. Huang, D. Yuan, C. Guo, J. Wang, Microstructure and Mechanical Properties of Low-Carbon High-Strength Steel Fabricated by Wire and Arc Additive Manufacturing, Metals (Basel). 10 (2020) 216. https://doi.org/10.3390/met10020216.

[53] B.E. Carroll, T.A. Palmer, A.M. Beese, Anisotropic tensile behavior of Ti–6Al–4V components fabricated with directed energy deposition additive manufacturing, Acta Mater. 87 (2015) 309–320. https://doi.org/10.1016/J.ACTAMAT.2014.12.054.

[54] J. Alcisto, A. Enriquez, H. Garcia, S. Hinkson, T. Steelman, E. Silverman, P. Valdovino, H. Gigerenzer, J. Foyos, J. Ogren, J. Dorey, K. Karg, T. McDonald, O.S. Es-Said, Tensile Properties and Microstructures of Laser-Formed Ti-6Al-4V, J. Mater. Eng. Perform. 20 (2011) 203–212. https://doi.org/10.1007/s11665-010-9670-9.

[55] M. Rafieazad, M. Ghaffari, A. Vahedi Nemani, A. Nasiri, Microstructural evolution and mechanical properties of a low-carbon low-alloy steel produced by wire arc additive manufacturing, Int. J. Adv. Manuf. Technol. 105 (2019) 2121–2134. https://doi.org/10.1007/s00170-019-04393-8.

[56] J. Bi, J. Shen, S. Hu, Y. Zhen, F. Yin, X. Bu, Microstructure and mechanical properties of AZ91 Mg alloy fabricated by cold metal transfer additive manufacturing, Mater. Lett. 276 (2020) 128185. https://doi.org/10.1016/J.MATLET.2020.128185.

[57] E. Farabi, T. Klein, M. Schnall, S. Primig, Effects of high deposition rate during cold metal transfer additive manufacturing on microstructure and properties of Ti-6Al-4V, Addit. Manuf. 71 (2023) 103592. https://doi.org/10.1016/J.ADDMA.2023.103592.

[58] L. Sun, F. Jiang, R. Huang, D. Yuan, C. Guo, J. Wang, Anisotropic mechanical properties and deformation behavior of low-carbon high-strength steel component fabricated by wire and arc additive manufacturing, Mater. Sci. Eng. A. 787 (2020) 139514. https://doi.org/10.1016/J.MSEA.2020.139514.

[59] C. V. Haden, G. Zeng, F.M. Carter, C. Ruhl, B.A. Krick, D.G. Harlow, Wire and arc additive manufactured steel: Tensile and wear properties, Addit. Manuf. 16 (2017) 115–123. https://doi.org/10.1016/J.ADDMA.2017.05.010.

[60] T.L. Anderson, Fracture mechanics: fundamentals and applications, CRC press, 2017.

[61] K. Pasewald, Erscheinungsformen von Rissen und Brüchen metallischer Werkstoffe/The Appearance of Cracks and Fractures in Metallic Materials, herausgegeben vom Verein Deutscher Eisenhüttenleute, 176 Seiten, 311 Bilder, Verlag Stahleisen GmbH, Düsseldorf 1996, DM 84,00, ISBN 3-514-00463-3, Mater. Corros. Und Korrosion. 48 (1997) 712–712. https://doi.org/10.1002/maco.19970481011.

[62] R.W. Hertzberg, R.P. Vinci, J.L. Hertzberg, Deformation and fracture mechanics of engineering materials, John Wiley & Sons, 2020.

[63] T. Zhang, H. Li, H. Gong, Y. Wu, A.S. Ahmad, X. Chen, Effect of rolling force on tensile properties of additively manufactured Inconel 718 at ambient and elevated temperatures, J. Alloys Compd. 884 (2021) 161050. https://doi.org/10.1016/J.JALLCOM.2021.161050.

7 APPENDIX

The summary results of the uniaxial tensile tests carried out in both longitudinal (Y) and transverse (Z) directions is further detailed in Table A. The data on the ER110S-G wire given by the manufacturer is also included for comparison.

Table A - Results from the uniaxial tensile tests performed in samples WAAM, HF80 and HF80-C

Sample Reference		UTS (MPa) $\mu \pm \sigma$	Yield strength (MPa) $\mu \pm \sigma$	Elongation to fracture (%) $\mu \pm \sigma$
WAAM	Y	915 ± 36	595 ± 33	20.8 ± 1.1
	Z	930 ± 13	591 ± 41	17.5 ± 1.0
HF80	Y	883 ± 9	607 ± 27	18.2 ± 2.6
	Z	878 ± 16	589 ± 18	17.1 ± 0.5
HF80-C	Y	876 ± 35	641 ± 61	16.0 ± 3.1
	Z	888 ± 13	635 ± 16	15.7 ± 1.8
Wire ER110S-G		790	710	20.0